

Chapter 2

The Oxygen Evolution Reaction: Mechanistic Concepts and Catalyst Design

Richard L. Doyle and Michael E.G. Lyons

2.1 Introduction

The splitting of water into hydrogen and oxygen is a vital component of a promising renewable energy infrastructure (Zhou 2005; Lewis and Nocera 2006). Hydrogen gas is regarded by many as the fuel of the future. With the highest mass energy density of any fuel and its clean combustion in air, hydrogen could be considered the ultimate clean energy carrier (Dinga 1985; Schlögl 2010). However, the realisation of a largely hydrogen based renewable energy solution—the hydrogen economy—depends heavily on the development of cost-effective, green production technologies (Crabtree et al. 2004). Hydrogen is readily produced on a large scale by steam reforming of natural gas, yet this non-renewable process is inherently environmentally offensive producing significant quantities of carbon dioxide (Häussinger et al. 2000). The catalytic splitting of water, on the other hand, offers a clean, renewable and potentially cost-effective route to the production of hydrogen gas (Ohi 2005; Tributsch 2008; Zeng and Zhang 2010).

R.L. Doyle (✉)

Electrochemical Materials and Energy Group, Tyndall National Institute,
University College Cork, Lee Maltings, Cork, Ireland
e-mail: richard.doyle@tyndall.ie

M.E.G. Lyons

Trinity Electrochemical Energy Conversion and Electrocatalysis Group,
School of Chemistry & AMBER National Centre, CRANN Research Institute,
Trinity College Dublin, Dublin 2, Ireland
e-mail: melyons@tcd.ie

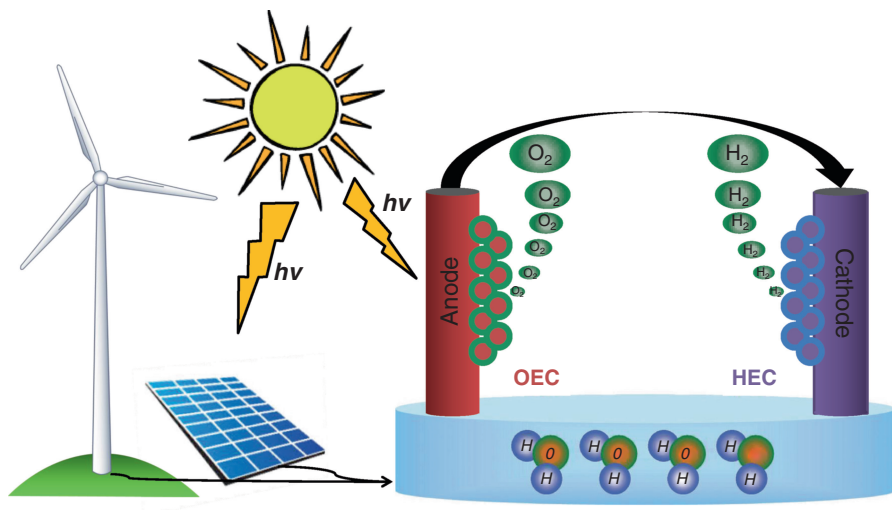
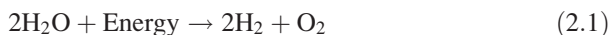


Fig. 2.1 Schematic representation of the splitting of water via electrolysis, utilising electricity derived from renewable sources such as wind and solar, and photoelectrolysis, where the electrodes directly harvest the solar energy. Oxygen evolution catalysts (OEC) are located on the anode and hydrogen evolution catalysts (HEC) are located on the cathode. Adapted from Joya et al. (2013)

In general, the overall water splitting process can be represented as follows, with molecular hydrogen and oxygen generated individually at the cathode and anode, respectively.



In principle, the energy required to drive the water splitting reaction can be obtained from any of a number of sources making it a highly versatile energy conversion technology, as illustrated in Fig. 2.1. One of the more attractive options is the coupling of electrochemical water splitting devices—water electrolyzers—with grid scale renewable energy harvesting technologies such as wind turbines or photovoltaics (Turner 2004; Grätzel 2005). In this way, water electrolysis could act as a local energy storage system permitting the implementation of these intermittent energy sources on a global scale (Lewis and Nocera 2006). An alternative method, in the context of solar-to-fuel conversion, is photoelectrolysis or light-driven water splitting (Brimblecombe et al. 2009; Nocera 2012; Joya et al. 2013). In this approach, light harvesting mechanisms, typically involving semiconductor materials, are incorporated into the electrode design so that the necessary solar energy is harvested directly by the electrode materials. Although technically more demanding than electrolysis from the point of view of electrode composition, this standalone approach is growing in popularity off the back of substantial progress in the design of artificial photosynthetic cells—the artificial

leaf (Nocera 2012; Joya et al. 2013). However, regardless of the route taken, the viability of these systems as sustainable hydrogen production technologies is, in the end, dependent on the electrochemistry of oxygen. The generation of molecular oxygen at the anode is the most energy-intensive step in the overall water splitting process (Hall 1983; Dau et al. 2010; Marinia et al. 2012).

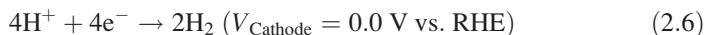
To understand this, consider the fundamental operating requirement of a water splitting system: the equilibrium potential V_{eq} of 1.23 V. In order to generate hydrogen at a specific rate, a voltage at least equal in magnitude to 1.23 V must be supplied to the system. For water electrolysis, this operational voltage depends on the kinetics of the water splitting reactions and the design of the electrolyser unit such that:

$$V_{\text{op}} = V_{\text{eq}} + \eta_{\text{A}} + |\eta_{\text{C}}| + \eta_{\Omega} \quad (2.2)$$

where η_{A} and η_{C} are the overpotentials required to overcome the kinetic barriers for the oxygen evolution reaction (OER) at the anode and the hydrogen evolution reaction (HER) at the cathode, respectively, and η_{Ω} is the additional overpotential required to compensate for resistance losses within the device (Trasatti 1994). The efficiency of the electrolyser unit is therefore reflected in the degree to which V_{op} deviates from V_{eq} . In an ideal system, η_{A} and η_{C} would be close to zero and V_{op} would depend only on η_{Ω} , which could be minimised through efficient design of the electrolyser unit. In reality, though, this is never the case and kinetic limitations are significant, accounting for up to 85 % of the total efficiency losses (Greeley and Markovic 2012). In alkaline solution, the OER and HER can be described by the following two electrochemical reactions:



and in acid the corresponding reactions are:



where V_{Anode} and V_{Cathode} are the equilibrium potentials for the OER and HER, respectively. In practice, the efficiency of water electrolysis is limited by the large anodic overpotential of the OER. Whereas the HER can proceed with appreciable currents at potentials close to its equilibrium potential (Markovic and Ross 2002; Sheng et al. 2010), the OER requires a substantial overpotential to generate measurable current densities. Consequently no working electrolysis device can approach the minimum operational voltage of 1.23 V (Greeley and Markovic 2012). Similarly, the slow kinetics of the OER complicate the design of photoelectrolysis devices. In direct light-driven water splitting it is not sufficient for the

band-gap of the semiconductor to just match the equilibrium potential for water splitting, it must also be large enough to easily overcome the OER overpotential if a reasonable rate is to be achieved (Valdés et al. 2012). Thus, understanding and optimising the oxygen evolution process is seen as one of the remaining grand challenges for both physical electrochemistry and energy science.

Bearing that in mind, this chapter focuses on the principles underlying efficient oxygen evolution electrocatalysis. Over the past fifty years, considerable research effort has been devoted to the design, synthesis and characterisation of oxygen evolution anode materials with the aim of achieving useful rates of active oxygen evolution at the lowest possible overpotentials. Owing to their stability under oxygen evolution conditions, metal oxides have emerged as the material of choice for catalysing the OER (Katsounaros et al. 2014). Even in the case of the solid metal electrodes, the anodic OER always occurs at an oxidised surface (Conway 1995). Accordingly, a wide range of oxide-based catalysts have been developed. Frequently, the leading OER anode materials are based on RuO_2 and IrO_2 , since these materials exhibit the lowest overpotentials for the OER at practical current densities (Michas et al. 1992). However, the high cost and low natural abundance of these materials renders their widespread commercial utilisation impractical (Kinoshita 1992). This fact has motivated an extensive search for earth abundant catalytic materials with a particular emphasis on the various oxides of first row transition metals (Fabbri et al. 2014; Galán-Mascarós 2015). Although they are typically unstable in acidic media, their relatively low cost and long term corrosion resistance in alkaline solution makes them attractive, alternative OER materials. Yet despite these efforts, OER catalysts are still predominantly developed by an intuitively trial and error approach. The type and method of preparation of the oxide along with its composition and surface morphology can all have a significant influence on its catalytic performance with the result that knowledge of the intrinsic activity of the material can remain elusive (Surendranath and Nocera 2012; Doyle et al. 2013). The central challenge for oxygen evolution research is, therefore, uncovering the mechanistic details and structural motifs necessary for efficient catalysis. Such a realisation could facilitate a unified theory of oxygen evolution catalysis, greatly accelerating the design of ever more efficient and cost effective catalysts.

Considering the extent of the research on oxide-based oxygen evolution catalysts, this chapter does not attempt an exhaustive review, but rather seeks to emphasise the key concepts common to these materials and to the study of the OER in general. The OER is fundamentally an electrocatalytic reaction and accordingly this chapter begins with a traditional electrochemical approach, outlining the practical and theoretical application of an ensemble of electrochemical techniques. This type of approach provides a valuable kinetic analysis of the OER upon which further mechanistic investigations should be based. In the second section of this chapter, modern computational descriptions of the OER are discussed. Theoretical calculations provide a thermodynamic basis for understanding the electrochemical activity of oxide materials and are a useful complement to a comprehensive experimental study. With the fundamental knowledge gained in these sections,

the chapter then progresses to consider OER catalyst design principles. In the third section, the contribution of single-parameter “descriptors” to the understanding of the intrinsic activity of OER catalysts is examined and in the fourth section, several prominent methods for enhancing the activity of OER catalysts are described. Taken together, these approaches form a multi-dimensional view of the requirements for efficient OER catalysis. Finally, this chapter concludes with a molecular level consideration of the nature of the OER active site at metal oxide catalysts that seeks to bridge the fields of heterogeneous electrocatalysis and homogeneous molecular catalysis.

2.2 Electrochemical Perspectives

Electrocatalysis can be broadly defined as the ability of an electrode material or surface to accelerate the rate of an electrochemical process. The core of any electrocatalytic study is therefore the elucidation of the kinetic parameters that describe the electron-transfer reactions at the interface. Key parameters of interest include the transfer coefficient and the corresponding Tafel slope, as well as the reaction orders of the mechanistically significant reactants. This section begins with a general overview of these important parameters focusing on practical considerations relating to their application in a kinetic study of the OER. Building on this, a simple electrochemical approach for the construction of a meaningful mechanistic interpretation of the OER is presented.

2.2.1 The Tafel Slope

In any electrochemical reaction, the fundamental observables are the current (i) and the potential (V). For a given interfacial process, the current is a manifestation of the rate of the interfacial reaction and can be shown to be dependent on the applied potential (Bard and Faulkner 2000). In essence, varying the potential is equivalent to changing the driving force for the electrode process (Surendranath and Nocera 2012). Thus, the relationship between the current and potential is a primary concern in electrocatalysis.

Steady-state Tafel plot analysis is the most widely applied technique in the study of electrocatalytic reactions. For a multistep reaction such as the OER, the relationship between the steady-state anodic current and the applied potential can be represented in the following general form:

$$i = i_0 \exp\left(\frac{\alpha_a F \eta}{RT}\right) \quad (2.7)$$

where i_0 is the exchange current which represents the rate of the forward and reverse reactions at the equilibrium potential, α_a is the transfer coefficient for the anodic reaction, η is the overpotential, F is Faraday's constant, R is the gas constant and T is temperature. This expression holds in the absence of mass transport limitations, which would alter the concentration of reactants at the electrode surface relative to their bulk values (Guidelli et al. 2014a, b). That is, the reaction is assumed to be under kinetic control. Now, if the current is expressed in logarithmic form, the Tafel relationship is revealed:

$$\log(i) = \log(i_0) + \eta/b \quad (2.8)$$

or alternatively, Eq. (2.8) can be expressed in the original format proposed by Tafel (1904):

$$\eta = a + b \log(i) \quad (2.9)$$

where a is a constant and b is the Tafel slope given by:

$$b = \frac{\partial \eta}{\partial \log i} = \frac{2.303RT}{\alpha_a F} \quad (2.10)$$

From Eqs. (2.8) and (2.9) it is clear that a linear relationship between η and $\log(i)$ is predicted such that the Tafel slope b , typically expressed in units of millivolts (mV) per decade of current (dec^{-1}), can be readily extracted from plots of $\log(i)$ vs. η or η vs. $\log(i)$.¹ It is noteworthy that substitution of the applied potential V for η has no impact on the measured Tafel slope and is often the preferred protocol for multistep reactions, where a particular reaction step may control the overall kinetic profile making it difficult to define the thermodynamic potentials for the individual steps (Surendranath and Nocera 2012).

The significance of the Tafel slope in electrocatalysis is multifaceted. Depending on the interpretation, it can provide the means for both a quantitative and mechanistic characterisation of an electrocatalytic process. At its most basic level, the Tafel slope is a sensitivity parameter giving a measure of the rate of increase of electrode potential or polarisation with the log of the current density. As such it is considered a useful parameter for the practical evaluation of electrocatalytic materials. Notably, Conway et al. (1987) contend that the Tafel slope is a more important measure of electrocatalytic performance than the commonly utilised i_0 , which is a measure of the intrinsic kinetic rate of a reaction. This is rationalised by the fact that

¹Traditionally Tafel plots were recorded using Galvanostatic methods where the current was controlled and the potential was measured, as described by Eq. (2.9). In this way, the Tafel slope could be obtained directly from the experimental plots, hence the convention of reporting the Tafel slope in the form of Eq. (2.10). However, due to the ease with which the potential can be controlled using modern potentiostats, Tafel plots are now routinely recorded in the form of Eq. (2.8) and the corresponding Tafel slope is obtained from the inverse slope of the experimental plot.

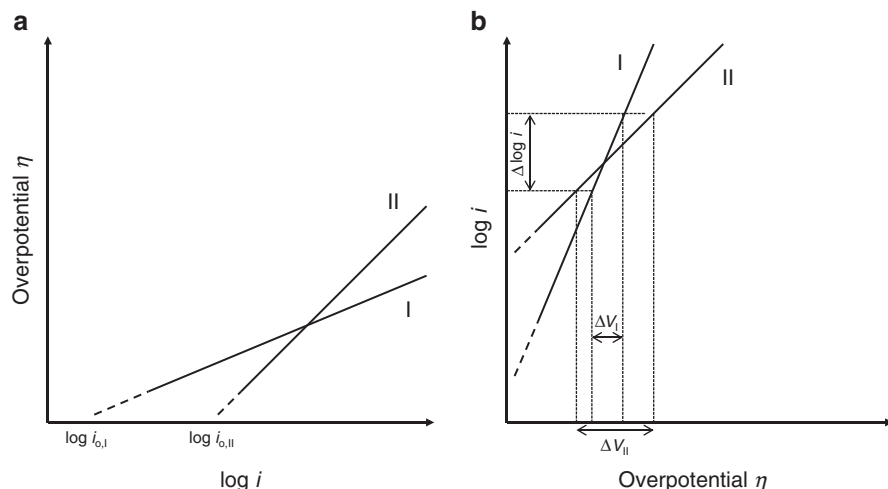


Fig. 2.2 Schematic diagrams illustrating the significance of Tafel slopes for determining favourable electrocatalytic properties. The quantities ΔV_I and ΔV_{II} indicate the potential changes necessary to alter the current output of catalyst I and II, respectively, by the value $\Delta \log i$. Adapted from Conway et al. (1987)

i_0 only refers to the kinetics at the thermodynamic potential and does not characterise the kinetics of the electrode process at higher, more practical current densities. This point is illustrated in Fig. 2.2 where schematic Tafel plots for catalytic materials with different i_0 and Tafel slope values are shown in the form of Eqs. (2.8) and (2.9). In Fig. 2.2a, catalyst I is depicted with a low i_0 value relative to catalyst II and so could be considered less active. However, catalyst II clearly has a larger Tafel slope than catalyst I, thereby experiencing greater polarisation with increasing current density. Consequently, catalyst I exhibits a lower overpotential than catalyst II at higher current densities. This distinction is particularly important for systems such as water electrolyzers where high current densities at minimum operational voltages are required for economic viability. In this respect, it should also be noted that such systems may require operation over a range of current densities depending on H_2 demand (Conway et al. 1987). Therefore, from a practical stand point, it is not just the current density obtainable at a given overpotential that is important but also the rate of change of this current density with overpotential—the inverse Tafel slope $1/b$ given by the slope of Eq. (2.8). As demonstrated in Fig. 2.2b, manipulation of the current density for catalyst I requires much smaller changes in overpotential than for catalyst II, making it a more practical real world material. Hence, low Tafel slopes are widely acknowledged as an indicator of efficient electrocatalytic performance (Conway et al. 1987; Merrill and Dougherty 2008).

Taking a more theoretical perspective, the Tafel slope yields insight into the mechanistic pathway of an electrode process. It can be seen from Eq. (2.10) that the

Tafel slope is defined by the transfer coefficient α_a which is experimentally quantifiable according to (Guidelli et al. 2014a, b):

$$\alpha_a = \frac{1}{b} \left(\frac{2.303RT}{F} \right) \quad (2.11)$$

Moreover, for a multistep reaction consisting of a sequence of elementary steps with a single rate determining step (RDS) α_a can be given by (Parsons 1951; Damjanovic et al. 1966, 1967a, b; Bockris and Khan 1993; Guidelli et al. 2014a, b):

$$\alpha_a = n_f / \nu + n_r \beta \quad (2.12)$$

where n_f is the number of electrons transferred before the RDS, ν is the stoichiometric number defined as the number of times the RDS occurs for one repetition of the overall reaction, n_r is the number of electrons transferred in each occurrence of the RDS and β is the symmetry factor. While there is no general consensus on the physical meaning of β it is related to the activation barrier and is generally assumed to be close to 0.5, describing a symmetrical potential energy barrier (Guidelli et al. 2014a, b). In this way, it can be seen that the Tafel slope is a composite parameter, giving information on the stoichiometry and the succession of steps in the overall reaction. Note, for an electron transfer step n_r can be safely assumed to equal one as the transfer of more than one electron at a time is improbable (Guidelli et al. 2014a, b). Therefore, if the first electron transfer step in a sequential reaction is rate-determining then $n_f = 0$ and $\alpha_a = \beta = 0.5$ implying a Tafel slope of 120 mV dec^{-1} . Similarly, if the second electron transfer step is rate-determining $n_f = 1$ and $\alpha_a = 1.5$, assuming a typical value of $\nu = 1$, giving a Tafel slope of 40 mV dec^{-1} . On the other hand, if the rate-determining step involves a chemical step subsequent to the first electron transfer step $n_r = 0$ and $n_f = 1$. In this case, $\alpha_a = 1$ predicting a Tafel slope of 60 mV dec^{-1} . Thus, the elucidation of Tafel slopes can be useful in differentiating between possible reaction mechanisms.

In view of the potential utility of the Tafel slope it is important to discriminate between true kinetic effects and experimental effects. The discussion so far has only considered the possibility of a single linear Tafel region. In practice, however, multiple Tafel regions may be observed. Certainly the presence of two distinct linear regions is a common kinetic feature of the OER Tafel plots presented in the literature (Damjanovic et al. 1966, 1967a; Hrussanova et al. 2004; Guerrini et al. 2007; Doyle and Lyons 2013a, b). Such changes in Tafel slope with increasing potential are most often attributed to either a change in the RDS within a given pathway or to the influence of changing potential on the adsorption of the reaction intermediates (Damjanovic et al. 1966, 1967a), the kinetic basis for which are discussed in Sect. 2.2.3. It is important though to note that increases in the Tafel slope do not necessarily have mechanistic significance and caution should be taken when interpreting multiple Tafel regions in terms of a possible mechanistic pathway. Experimentally, increases in the Tafel slope with applied potential could be the result of a reduction in the effective electrode surface area with increasing gas

evolution at the higher applied potentials. Likewise, the onset of mass transport limitations at high overpotentials will reduce the sensitivity of the current response to increases in potential resulting in an increasing Tafel slope. These complications can be readily minimised using a rotating disc electrode which would simultaneously limit the adherence of gas bubbles to the electrode surface while providing a well-defined mass transport regime.

However, the identification of true mechanistically significant changes in Tafel slope is best accomplished using a combination of experimental techniques. Tafel plots can be generated using various steady-state polarisation techniques, Impedance Spectroscopy (IS) and the analysis of open circuit potential decay curves, the specific details of which have been comprehensively reviewed by Doyle et al. (2013). IS offers a useful accessory method for the determination of Tafel slopes. Obtaining equivalent Tafel slopes using IS involves the experimental measurement of the total Faradaic resistance R_{far} as a function of the applied potential according to:

$$\log\left(\frac{1}{R_{\text{far}}}\right) = \frac{V}{b} + \log\left(\frac{2.303i_0}{b}\right) \quad (2.13)$$

implying that the inverse slope of a plot of $\log(1/R_{\text{far}})$ against V is equal to the Tafel slope b . In this regard, the following caveat should be noted; the parameter R_{far} is a combination of the charge transfer resistances for all steps in the reaction, regardless of whether they are the RDS, a preceding step or a following step and so mechanistic interpretation of IS Tafel slopes alone is not recommended (Harrington and van den Driessche 2011). That said, a number of studies have highlighted the effectiveness of this type of data treatment when used along side steady-state polarisation techniques (Lyons and Brandon 2009; Doyle and Lyons 2013a, b). A comparison of the steady-state polarisation and IS Tafel plots obtained for a hydrous iron oxide catalyst is presented in Fig. 2.3a. Clear agreement was observed between the two different methods and in this situation, the authors could conclude that the dual Tafel behaviour was in fact mechanistically significant and not simply due to electrode blocking, mass-transport limitations or ohmic effects (Doyle and Lyons 2013a, b).

Steady-state measurements are also complemented by studies of the decay of the open circuit potential (OCP). This approach is frequently adopted in cases where elucidation of the reaction mechanism by steady state polarisation techniques is complicated by continuous alteration of the electrode surface with time. Following an initial polarisation at a potential in the region where OER Tafel behaviour is observed, the variation of the electrode potential at open circuit with time is given by (Bockris et al. 2002):

$$V_{\text{OCP}} = \frac{2.303RT}{\beta F} \log\left(\frac{RT}{\beta F i_0}\right) - \frac{2.303RT}{\beta F} \log(t) \quad (2.14)$$

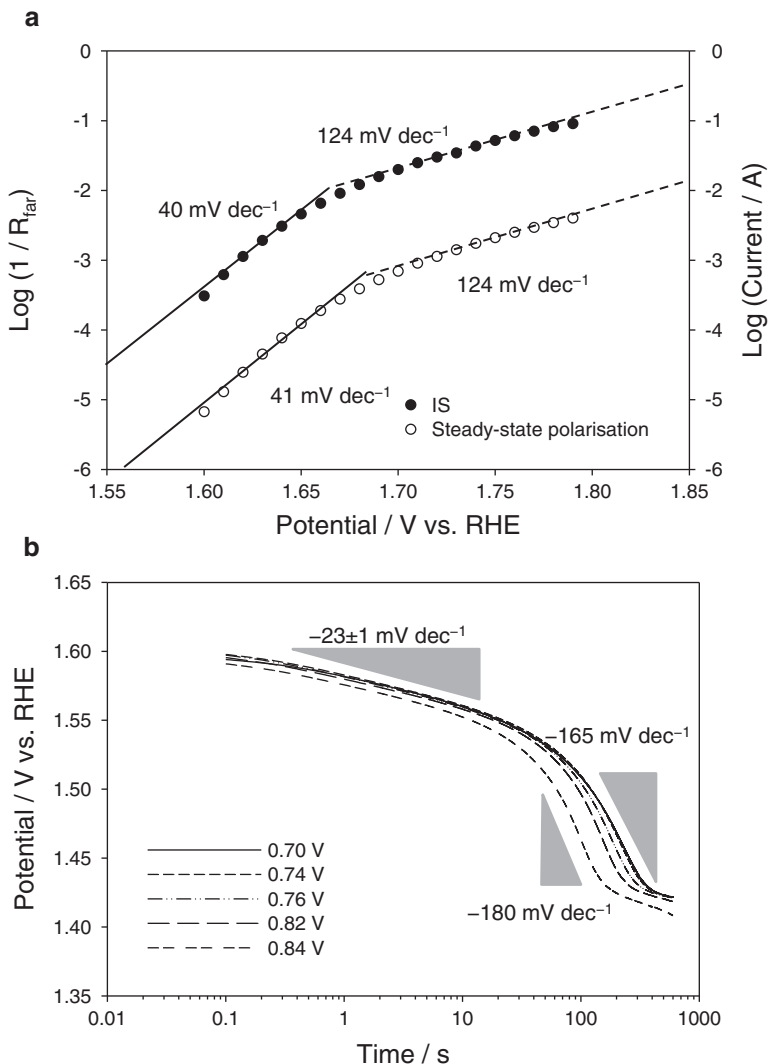


Fig. 2.3 (a) A comparison of the Tafel plots generated using IS and steady-state polarisation data and (b) the variation of OCP as a function of log (time) after a 5 min polarisation period at a series of potentials associated with oxygen evolution for a hydrous iron oxide catalyst film in 1.0 M NaOH. Adapted from Doyle et al. (2013)

On this basis, the slope b_{OCP} of a plot of the measured potential or overpotential during the decay as a function of $\log t$ is equal to the negative of the Tafel slope b (Bockris et al. 2002). While such simple relationships between the OCP decay slope and the Tafel slope have certainly been observed (Lyons and Floquet 2011), the true power of this approach lies in its ability to describe the potential dependence of the surface capacity and the fractional coverage of surface

intermediates. In deriving Eq. (2.14) it was assumed that the electrode surface capacitance is independent of potential (Bockris et al. 2002). In fact, Conway and Bourgault (1959, 1962) and Bourgault and Conway (1960) have shown that this is the only case under which Eq. (2.14) holds. Thus, the observation of numerical identity between the decay slope and the Tafel slope suggests that the surface capacity remains constant during self-discharge. In situations where the surface capacity varies during self-discharge the observed decay slope can differ quite significantly from the steady-state Tafel slope. This is evident in Fig. 2.3b where the corresponding V vs. $\log t$ plots for the hydrous iron oxide catalyst are shown. At short decay times a slope b_{OCP} of ca. -23 mV dec^{-1} is obtained, whereas at longer times the slope b_{OCP} varies between ca. -160 and -180 mV dec^{-1} depending on the initial polarisation potential. Importantly, these slopes differ considerably from the expected slope of ca. 40 mV dec^{-1} obtained using steady-state polarisation and IS techniques in Fig. 2.3a. To interpret this result two primary limiting cases can be identified from the analysis of Conway and Bourgault (1962). If the surface coverage of intermediates during self-discharge is assumed to be low, it can be shown that the surface capacity decreases with decreasing potential giving the following relationship between the decay slope b_{OCP} and the true Tafel slope b :

$$b_{\text{OCP}} = \frac{b'b}{b - b'} \quad (2.15)$$

where b' is some positive multiple or fraction of RT/F . Hence the observed decay slope is predicted to be greater than the Tafel slope. Conversely, if there is high but not full coverage of intermediates the surface capacity increases with decreasing potential and the decay slope is given by:

$$b_{\text{OCP}} = -\frac{b'b}{b' - b} \quad (2.16)$$

indicating that the observed decay slope will be less than the Tafel slope. In this way, the lack of agreement between the decay slopes and Tafel slopes in Fig 2.3 suggests that the surface capacity does not remain constant during self-discharge. This was interpreted in terms of a decrease in the surface concentration of charged *surfaquo* groups, which were considered to be the active sites for oxygen evolution (see Sect. 2.5.4) (Doyle et al. 2013). From an accompanying IS study, these authors found that the surface capacity increased with increasing potential in accordance with the formation of charged surface intermediates (Doyle and Lyons 2013a, b). Therefore, following the reasoning of Conway and Bourgault (1962), at high potentials or short decay times a large proportion of the *surfaquo* groups are in the higher charged state implying significant surface coverage of intermediates and the observed decay slope is lower than the Tafel slope. On the other hand, for longer times the surface coverage becomes considerably reduced due to increased

discharge² of the *surfaquo* groups and the decay slope is found to be greater than the Tafel slope. In this way, the relationship between the decay slope and the steady state Tafel slope can provide a useful qualitative characterisation of the kinetics and mechanism of the basic processes involved in an electrocatalytic reaction.

2.2.2 Electrochemical Reaction Orders

The relevance of reaction orders in the kinetic study of chemical reactions is well known. Their determination provides the relationship between the reaction rate and the concentration of a particular reactant—a key criterion used in mechanistic interrogations. In the case of electrochemical reactions, the rate of the reaction, expressed as current, is intimately related to the applied potential, as described in Sect. 2.2.1. As a result, the electrochemical reaction order m_x can be expressed in terms of either of these quantities according to the following derivatives (Conway and Salomon 1964):

1.

$$m_{x,i} = \left(\frac{\partial V}{\partial \log a_x} \right)_i$$

2.

$$m_{x,\eta} = \left(\frac{\partial \log i}{\partial \log a_x} \right)_\eta$$

3.

$$m_{x,V} = \left(\frac{\partial \log i}{\partial \log a_x} \right)_V$$

where a_x is the activity of a mechanistically significant reactant x and the subscripts i , η , and V denote conditions of constant current, constant overpotential, and constant applied potential, relative to a pH independent reference electrode, respectively. It should be noted that the parameter $m_{x,V}$ is regarded as the “chemically” or “mechanistically” significant reaction order since it gives the dependence of $\log(\text{rate}/i)$ on $\log(\text{reactant concentration}/a_x)$ in the absence of variations of the double-layer configuration, i.e. constant V (Conway and Salomon 1964). In contrast to the situation outlined in Sect. 2.2.1 for the Tafel slope, substitution of the potential for the overpotential is not innocent with regard to measured reaction orders and the following correction factor is necessary to account for this (Lyons et al. 2014; Gileadi 1993):

² Self-discharge is assumed to proceed by an electrochemical mechanism analogous to that of corrosion. That is, the simultaneous occurrence of anodic and cathodic reactions as a mixed potential via a local cell mechanism. In the present case, self-discharge consists of a cathodic oxide or *surfaquo* group reduction process and an anodic oxygen evolution process.

$$m_{x,\eta} = m_{x,V} - \beta \quad (2.17)$$

In addition, the relationship between $m_{x,i}$ and $m_{x,V}$ offers a useful self-consistency check³ between the experimentally measured Tafel slope b and the mechanistically significant reaction order $m_{x,V}$ as follows (Surendranath and Nocera 2012):

$$m_{x,i} = -b(m_{x,V}) \quad (2.18)$$

However, in subsequent discussions all references to the parameter m_x refer to the mechanistically significant $m_{x,V}$.

In the case of alkaline water electrolysis the pertinent reactant term is the activity of the hydroxide ion a_{OH^-} . Thus, a plot of $\log i$ vs. $\log a_{\text{OH}^-}$ should be linear with slope equal to the corresponding electrochemical reaction order m_{OH^-} . These experimentally determined reaction order values can often be potential dependent and so it is necessary to generate reaction order plots at a range of potentials. This is especially important for systems exhibiting dual Tafel behaviour, as distinct reaction orders can be associated with each Tafel region. A sample reaction order study for a hydrous iron oxide catalyst is shown in Fig. 2.4. An important point which must be considered when interpreting such reaction order data is that, theoretically, reaction orders should be integer values. While the reaction orders in Fig. 2.4 are statistically close to unity, this is not always the case and fractional reaction orders can often be observed. Simply, a reaction order $m_{\text{OH}^-} = 1$ suggests that only a single hydroxide ion reacts at each active site for all steps up to and including the RDS. Similarly, if $m_{\text{OH}^-} = 2$ then a total of two OH^- equivalents can be assumed to be involved in the overall reaction prior to and including the RDS. However, it can be more difficult to rationalise fractional reaction orders. A number of authors have considered the effect of the diffuse layer potential ϕ^* on the observed kinetic parameters (Parsons 1961; Alberly 1975; Lyons and Floquet 2011). Here, the diffuse layer corrected electrode potential is represented by $V - \phi^*$ where:

$$\phi^* = \frac{RT}{F} \ln a_x \quad (2.19)$$

and $a_x = a_{\text{OH}^-}$ or a_{H^+} depending on the medium. Thus, if the experiments are not performed at a constant ionic strength then the observed reaction order might not correspond to a constant $V - \phi^*$. For example, Lyons and Floquet (2011) suggest that correcting for the diffuse layer potential can account for the fractional reaction order $m_{\text{H}^+} = -1.5$ observed for RuO_2 layers in acidic media. On the other hand, Carugati et al. (1981) have proposed that fractional reaction orders may arise due to competing or parallel reaction pathways. In such cases, the experimentally

³ Applying this check to the low Tafel slope data in Fig. 2.4 gives $m_{x,i} = -(0.058)(1.01) = -0.059$, in agreement with the slope of -0.057 obtained for a plot of V measured at 1.0 mA cm^{-2} versus $\log a_{\text{OH}^-}$.

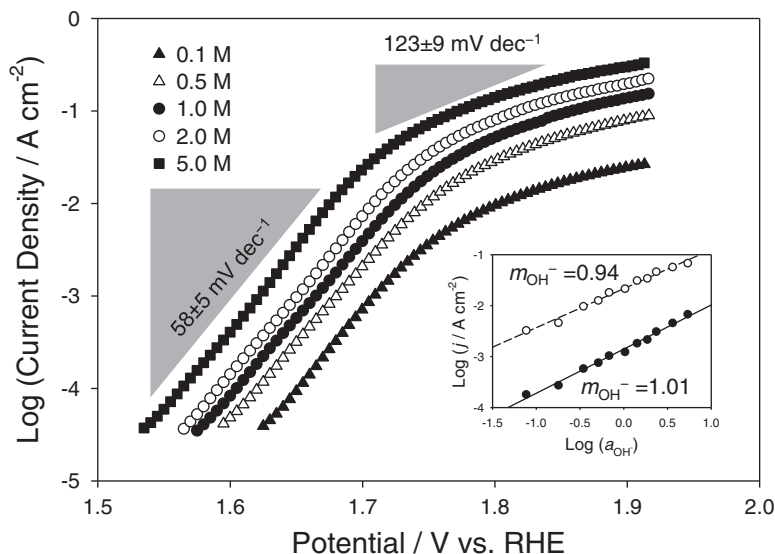


Fig. 2.4 Steady-state polarisation curves recorded for a hydrous iron oxide catalyst film in a series of aqueous NaOH solutions of varying concentrations. The Tafel regions are indicated by the *triangular features*. Reaction order plots generated at fixed potentials in the low and high Tafel regions are shown in the *inset*. Adapted from Doyle and Lyons (2013)

observed kinetic parameters represent a combination of the parameters expected for the competing pathways, the exact value of which depends on the fraction of catalytic sites following each individual pathway. Then again, fractional reaction orders can also arise depending on the surface coverage of intermediates. Bockris and Ottagawa (1983) observed a reaction order of $m_{\text{OH}^-} = 1.5$ for a range of cobalt perovskites whereas Lyons and Brandon (2009) reported the same value for “aged” passive iron oxides. In both cases it was shown that the fractional reaction orders could be rationalised by admitting Temkin rather than Langmuir adsorption conditions.

2.2.3 Mechanistic Analysis

In terms of a mechanistic analysis of the OER, a major difficulty lies in the fact that the OER is a complex process involving the transfer of four electrons. Since electrons are transferred one at a time the process will, by necessity, be multistep in which distinct intermediates are generated on the electrode surface. Consequently, the OER may follow any of a number of different pathways. In this respect, evaluation of the parameter couple (b, m_{OH^-}) will go a long way towards narrowing the possible mechanistic pathways.

Over the years various possible mechanistic schemes have been proposed with notable early studies including the works of Bockris and Otagawa (1983), Krasil'shchikov (1963), Kobussen and Broers (1981), Willems et al. (1984) and O'Grady et al. (1974). In these early mechanistic schemes the OER was usually interpreted in terms of an initial discharge of hydroxide ions at a catalytically active surface site M leading to the formation of discrete adsorbed hydroxide intermediates:



Subsequent steps in the reaction were thought to involve the formation of a range of surface adsorbed intermediates such as MO, MOOH or physisorbed peroxide species, which could then react with each other, through various disproportionation or bimolecular decomposition reactions, or undergo nucleophilic attack from the electrolyte to liberate oxygen gas (Dau et al. 2010; Marinia et al. 2012). A summary of the diagnostic criteria for some of these commonly considered pathways is presented in Table 2.1.

In order to derive a rate expression for the OER, and thereby distinguish between reaction pathways, it is useful to view the overall reaction as a sequence of elementary one electron transfer steps and chemical steps. From this perspective, the overall rate of the OER can be expressed in terms of the slowest step or RDS. Depending on which particular elementary step is rate-limiting, the reaction sequence can predict several different Tafel slope and reaction order values. By way of illustration consider the Bockris Electrochemical Oxide Path in Table 2.1. If step 2 (II-2) in this scheme is the RDS then the net reaction flux f_2 for pathway II is given by:

$$f_\Sigma \cong f_2 = i/4FA = k_2^0 a_{\text{OH}^-} \theta_{\text{MOH}} \exp[\beta F \eta / RT] \quad (2.21)$$

where f_2 and k_2^0 are the reaction flux and standard rate constant, respectively, for the forward reaction in II-2 and θ_{MOH} is the fractional surface coverage of the intermediate MOH. That is, θ_{MOH} represents the proportion of the total number of active sites M that exist in the intermediate state MOH under steady-state conditions. Now, if there is a high surface coverage of intermediates, MOH will be the dominant surface species and θ_{MOH} can be said to approach unity, $\theta_{\text{MOH}} \rightarrow 1$. In this case, θ_{MOH} is treated as a constant and the net reaction flux (Eq. (2.21)) predicts a reaction order $m_{\text{OH}^-} = 1$ and a Tafel slope $b = 2.303(2RT/F)$ or 120 mV dec⁻¹, assuming $\beta = 0.5$.

On the other hand, if there is a low surface coverage of intermediates, M will be the dominant surface species and $\theta_{\text{MOH}} \rightarrow 0$ as $\theta_{\text{M}} \rightarrow 1$. In this case, it is necessary to express the term θ_{MOH} in Eq. (2.21) in terms of the constant θ_{M} . This can be accomplished in one of two ways. The first method, the quasi-equilibrium method, assumes that only the RDS is irreversible and all other steps are in equilibrium (Guidelli et al. 2014a, b). Under these conditions, the rate of the forward and reverse reactions in II-1 should be equal with reaction fluxes given, respectively, by:

3. $2M^{z+}OH + 2OH^- \rightarrow M^z + H_2O + O_2$	1	RT/4F	∞	4	2	RT/2F	RT/F	4	3	$K_2 \sim 1$
(V) Kobussen's Path (Kobussen and Broers 1981, Willems et al. 1984)						RT/4F	RT/3F	4	3	$K_2 \ll 1$
1. $M + OH^- \rightarrow MOH + e^-$	1	2RT/F		1						
2. $MOH + OH^- \rightarrow MO + H_2O + e^-$	1	2RT/3F	2RT/3F	2	1	2RT/F		1		$r_{OH} \sim r_O$
						RT/F		1.5		$r_{OH} \gg r_O$
3. $MO + OH^- \rightarrow MO_2H^-$	1	RT/2F	∞	3	1	∞		1		$K_2 \sim 1$
						RT/F		2		$K_2 \ll 1$
4. $MO_2H^- + OH^- \rightarrow MO_2^- + H_2O + e^-$	1	2RT/5F	2RT/F	4	1	2RT/F		1		$K_3 \sim 1$
						2RT/F		2		$K_3 \ll 1$
5. $MO_2^- \rightarrow M + O_2 + e^-$	1	2RT/7F	∞	4	0	RT/F	2RT/F	1	0.5	$K_4 \sim 1$
						RT/2F	2RT/3F	1	1.5	$K_4 \ll 1$

^aSymmetry factors, i.e. β , γ and δ , in all steps, were taken as $\frac{1}{2}$

^b ζ is the potential difference between the outer Helmholtz plane and the bulk of the solution

^cStoichiometric number

^dNonactivated desorption of O_2

^eActivated desorption of O_2

^f r is a coefficient determining the variation of heat of adsorption of a particular species with coverage. Unless stated, r values for each species were taken as equal. K_i is the equilibrium constant of the i th step

^g r_1 and r_2 refer to r for M^zOH and r for $M^{z+1}OH$, respectively

$$f_1 = k_1^0 a_{\text{OH}^-} \theta_{\text{M}} \exp[\beta F \eta / RT] \quad (2.22)$$

and,

$$f_{-1} = k_{-1}^0 \theta_{\text{MOH}} \exp[-(1 - \beta) F \eta / RT] \quad (2.23)$$

Applying the equilibrium condition $f_1 = f_{-1}$ and rearranging gives the following expression for θ_{MOH} :

$$\theta_{\text{MOH}} = K a_{\text{OH}^-} \theta_{\text{M}} \exp[F \eta / RT] \quad (2.24)$$

where $K = k_1^0 / k_{-1}^0$. Now substituting for θ_{MOH} in Eq. (2.21), the net reaction flux can be readily estimated as:

$$f_{\Sigma} \cong k_2^0 (a_{\text{OH}^-})^2 \theta_{\text{M}} \exp[(1 + \beta) F \eta / RT] \quad (2.25)$$

Thus, under low surface coverage of intermediates the predicted reaction order and Tafel slope are now $m_{\text{OH}^-} = 2$ and $b = 2.303(2RT/3F)$ or 40 mV dec⁻¹ respectively.

Alternatively, the steady-state method can be used to provide an expression for θ_{MOH} . According to this method, a short time after initiation of the process, the effective concentrations of all intermediates are assumed to reach values that remain constant in time and therefore, are in a steady state. This implies that the rate of formation and disappearance of any intermediate will be equal, with the result that the rate of change of its concentration will be zero (Guidelli et al. 2014a, b). Applying this condition to θ_{MOH} gives:

$$\frac{d\theta_{\text{MOH}}}{dt} = f_1 - f_{-1} - f_2 \cong 0 \quad (2.26)$$

where the rate of formation of θ_{MOH} is given by f_1 and the rate of its disappearance is $f_{-1} + f_2$. Here, substituting for f_1, f_{-1} and f_2 in Eq. (2.26) and again rearranging for θ_{MOH} gives:

$$\theta_{\text{MOH}} = \frac{k_1^0 a_{\text{OH}^-} \theta_{\text{M}} \exp[\beta F \eta / RT]}{k_{-1}^0 \exp[-(1 - \beta) F \eta / RT] + k_2^0 a_{\text{OH}^-} \exp[\beta F \eta / RT]} \quad (2.27)$$

At first glance it appears that the quasi-equilibrium and steady-state methods are inconsistent. However, noting that II-2 is the RDS, it is safe to assume that $k_2^0 \ll k_{-1}^0$. In fact, this assumption is implicit in the quasi-equilibrium method, where the rate constant of the RDS is required to be at least 100 times smaller than those of all steps that precede it (Guidelli et al. 2014a, b). Thus, Eq. (2.27) reduces to Eq. (2.24) and the same expression for the net reaction flux in Eq. (2.25) is obtained.

Hence, distinct kinetic parameters are predicted for low and high surface coverage of intermediates. Further coverage effects can also be considered. Several studies have utilised a Temkin isotherm to describe the adsorption process (Parsons 1958; Thomas 1961; Conway and Gileadi 1962; Bockris and Otagawa 1983; Lyons and Brandon 2009). The limiting coverages $\theta \rightarrow 0$ and $\theta \rightarrow 1$, known as Langmuir adsorption conditions, operate under the assumption that lateral interactions between adsorbed species have no effect on the reaction kinetics. However, for intermediate coverages ($0.2 < \theta < 0.8$) where no single species can be said to be dominant it is reasonable to expect the interactions between adsorbates to be significant. Such cases are best described in terms of a Temkin isotherm. For example, Conway and Gileadi (1962) outlined a model based on the principle that the free energy of adsorption of an intermediate species depends on the total fractional coverage of all adsorbed reaction intermediates as follows:

$$\Delta G_\theta = \Delta G^0 - r_x \theta \quad (2.28)$$

where ΔG_θ and ΔG^0 are the adsorption free energies of an intermediate species x in the presence and absence of coverage effects, respectively, and r_x is the rate of change in the free energy of adsorption with the total coverage. According to this model, the free energy of adsorption of an intermediate will decrease with increasing total fractional coverage. For a reaction step consisting of the inter-conversion of two adsorbed intermediates such as II-2, a decrease in the free energy of adsorption of the intermediate species MO with increasing total coverage would result in an increase in the free energy of activation for II-2. In contrast, a decrease in the free energy of adsorption of MOH would cause a decrease in the activation energy. The overall reaction kinetics will, therefore, be influenced by changes in the relative populations of important intermediates. In particular, depending on the relative sensitivities of the free energy of the intermediates to changes in surface coverage, as expressed through their respective r values, further distinct kinetic parameters can be estimated. Sample kinetic analyses under Temkin conditions are outlined by Bockris and Otagawa (1983) and Lyons and Brandon (2009), and the predicted kinetic parameters for II-2 are presented in Table 2.1.

The above discussion is predicated on a slow electron-transfer step determining the overall kinetics of the OER. However, a slow chemical step can equally be rate-limiting. The reaction step in II-2 represents a proton coupled electron transfer. This step could also be decomposed into a sequential proton transfer and electron transfer process as follows:



Indeed, this is the only difference between the Bockris Electrochemical Oxide Path and Krasil'shchikov's Path. It can be seen in Table 2.1 that III-2 and III-3 are the

equivalent of Eqs. (2.29) and (2.30). In this case, if Eq. (2.29) is the slow step then the reaction flux expression (Eq. (2.21)) can be modified to give:

$$f_{\Sigma} \cong i/4FA = k_2 a_{\text{OH}^-} \theta_{\text{MOH}} \quad (2.31)$$

Note k_2 is now a chemical rate constant and there is no potential dependence. Under low coverage Langmuir adsorption conditions θ_{MOH} is again replaced by Eq. (2.24) resulting in the following estimate for the net reaction flux:

$$f_{\Sigma} \cong k_2 (a_{\text{OH}^-})^2 \theta_{\text{Mexp}} [F\eta/RT] \quad (2.32)$$

Thus, if a chemical step, such as the reaction outlined in Eq. (2.29), rather than an electron-transfer step is rate-limiting a reaction order $m_{\text{OH}^-} = 2$ and Tafel slope $b = 2.303(RT/F)$ or 60 mV dec⁻¹ are predicted.

In this way, the determination of Tafel slopes and electrochemical reaction orders provides valuable insight into the rate-limiting processes at the reaction interface. It is clear that these reaction parameters are strongly influenced by the concentration and interaction of the surface species generated during the OER. This provides a kinetic basis for the rationalisation of multiple experimental Tafel regions. An assumption implicit in the analysis thus far is that a single isotherm can describe the surface coverage of key intermediates. Over short potential ranges such an assumption will likely hold; it has been pointed out by Damjanovic et al. (1966, 1967a) that the range of potentials over which Temkin conditions might be expected to prevail is limited to ca. 150 mV. Over wider potential ranges it is more realistic to expect the surface coverage to vary appreciably. Consider the situation where II-2 is rate determining, the relative proportion of active sites in the MOH state is controlled primarily by the equilibrium in step II-1. Given that II-1 involves the transfer of one electron, one could easily suppose the equilibrium to favour the formation of the MOH species at high overpotentials. Accordingly, the surface coverage of a particular intermediate could be potential dependent, transitioning through states of low, intermediate and high coverage over the course of a polarisation experiment. Examining the simplest case where θ_{MOH} changes from low coverage to high coverage with increasing potential, this transition would be characterised by a change in Tafel slope from 40 to 120 mV dec⁻¹ with a corresponding change in reaction order from $m_{\text{OH}^-} = 2$ to $m_{\text{OH}^-} = 1$. Interestingly, this dual Tafel behaviour could also be accounted for by a change in RDS. If step II-1 becomes rate-limiting at high overpotentials then the net reaction flux is given simply by Eq. (2.22) which can be readily shown to predict a Tafel slope of 120 mV dec⁻¹ and a reaction order $m_{\text{OH}^-} = 1$. In such cases, concurrent IS and OCP decay analysis can be useful in distinguishing between surface coverage effects and a change in the RDS. As noted in Sect. 2.2.1, variations in the oxide surface capacity during active oxygen evolution reflect the changing concentration of surface intermediates (Terezo et al. 2001; Klahr et al. 2012a, b) (see also Chap. 7). Thus, significant increases in the oxide surface capacity with increasing potential, as measured by IS, or large deviations of the OCP decay slope from the

Tafel slope would point to changes in the surface coverage of intermediates rather than a change in the RDS being the reason behind the dual Tafel behaviour.

The foregoing kinetic analysis highlights an inherent complication in attempts at a mechanistic analysis of the OER. That is, the kinetic parameters predicted for a particular pathway are not unique. Hence it is often very difficult to unambiguously identify the pathway operative for a particular system. Combining electrokinetic studies with a more detailed interrogation of the reactive interface is essential for the development of a complete mechanistic picture. Cyclic voltammetry studies of the surface redox characteristics of an oxide electrode are useful for diagnosing changes in the surface structure prior to the onset of catalytic activity, whereas *in situ* and *ex situ* spectroscopic studies can provide insight into the nature of the catalytically active surface. Modern studies of the OER often rely on such a multidisciplinary approach and several prominent examples are discussed in Sect. 2.5.

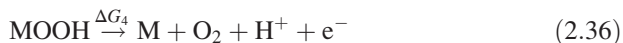
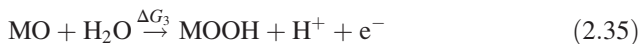
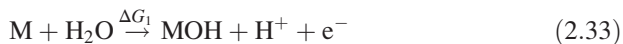
Nevertheless, the kinetic approach described here is of fundamental value in the study of the OER on transition metal oxides. Although it is not possible to isolate a single reaction pathway with the exclusion of all others, identification of the rate-determining step provides an important mechanistic foundation. Optimising electrocatalytic activity is a matter of achieving the highest possible current at the lowest possible overpotential. Low Tafel slopes are therefore an essential requirement for OER electrocatalysts. From this simple observation one can begin to formulate the principles for catalyst design. With reference to the mechanisms in Table 2.1 low Tafel slopes are associated with steps other than the primary discharge step being rate-determining. From this perspective, facilitating the discharge step offers an opportunity for catalyst enhancement; if the stability of the adsorbed intermediate formed in the primary discharge step can be increased then the rate control will shift to a later step. Thus, low Tafel slopes can be achieved through the interaction of strongly adsorbed surface intermediates (Hoare 1967, 1968). An alternative view point is highlighted in the mechanism of O'Grady et al. (1974) in Table 2.1, who emphasised the importance of oxide redox transitions in the course of the OER. In this concept, the OER is facilitated by the cyclic formation and decomposition of an unstable intermediate containing a metal centre in a higher valence state ($z + 1$) than its initial state (z) (O'Grady et al. 1974; Burke et al. 1982a). The significance of this approach lies in its ability to account for low experimental Tafel slopes without the need to consider strong surface adsorption; instead the activity of the surface oxide is linked to its stability. Despite their humble origins, these electrocatalytic concepts remain at the forefront of modern mechanistic interpretations of OER activity and will be explored in greater detail throughout the remainder of this chapter. In Sect. 2.3, the electrochemical activity of transition metal oxides for the OER is examined from a theoretical perspective.

2.3 Thermochemical Perspectives

In recent years, the oxygen evolution reaction on metal oxide surfaces has been widely studied using theoretical methods. As a complex, multistep, inner sphere process, the OER depends critically on the formation and stabilisation of high-energy surface-confined intermediates. Detailed knowledge of the interaction between the catalyst surface and the reaction intermediates is therefore essential if a fundamental understanding of the OER is to be developed. These issues are often difficult to address experimentally due to short lifetimes of reaction intermediates, harsh reaction conditions and extensive gas evolution at the surface of interest. Theoretical approaches, on the other hand, are very constructive as they allow one to access individual reaction steps and reaction intermediates. Although the complexity of the oxide surface makes accurate computation a challenging task, a simple thermochemical framework has emerged providing insights into the origin of the OER overpotential and the viable mechanistic paths.

2.3.1 The Potential-Determining Step

Over the past 10 years, extensive work by the groups of Nørskov and Rossmeisl has led to the development of an effective method for modelling the thermochemistry of electrochemical reactions (Rossmeisl et al. 2005; Rossmeisl et al. 2007a; Nørskov et al. 2009; Valdés et al. 2012). This model utilises quantum chemical calculations based on Density Functional Theory (DFT) to determine the thermodynamics of the separate reaction steps in a catalytic mechanism. Applying this method to the OER, they considered the following model reaction mechanism, termed the “associative” mechanism (Rossmeisl et al. 2007a):



where ΔG_i is the Gibbs free reaction energy of reaction step i . Note each reaction step involves the transfer of one electron implying the free energy change for each step will be potential dependent. Also, while this mechanism describes the OER under acidic conditions, the thermodynamic conclusions are independent of pH as the free energies deduced from Eqs. (2.33) to (2.36) vary in the same way with pH (Valdés et al. 2012). In their theoretical framework, Rossmeisl et al. (2007a)

calculated the Gibbs free adsorption energies of the surface intermediates ΔG_{MOH} , ΔG_{MO} , and ΔG_{MOOH} as a function of the electrode potential. At a given applied potential, the reaction energy of each elementary mechanistic step was given by the difference between the adsorption energies of two intermediates. For example, ΔG_3 depends on the relative free energies of the MO and MOOH intermediates according to: $\Delta G_3 = \Delta G_{\text{MOOH}} - \Delta G_{\text{MO}} - qV$. In this way, reaction free energy diagrams were generated allowing the identification of the thermodynamically least favourable step in the reaction path (Rossmeisl et al. 2005, 2007a).

Sample free energy diagrams for two hypothetical catalysts are plotted at different potentials in Fig. 2.5. The horizontal lines represent the free adsorption energies of the individual intermediates and the reaction coordinate moves from free water on the left to free O_2 on the right. For a typical electrocatalyst, the reaction energies for each step will differ due to irregular variations in the adsorption energies of the intermediate species (Dau et al. 2010). This situation is depicted by the “Real” catalyst trace in Fig. 2.5 where $\Delta G_3 > \Delta G_1 = \Delta G_2 > \Delta G_4$. As one might expect, all steps in the reaction are thermodynamically unfavourable at potentials below the reversible potential, $V_1 - V^0 = \eta < 0$, with $\Delta G_i > 0$. As the potential is increased, the free energies of the intermediates shift negatively so that the reaction steps eventually become thermodynamically favourable with $\Delta G_i \leq 0$. However, due to differences in the adsorption energies of the intermediates, each individual ΔG_i value will turn negative at a different potential. In Fig. 2.5 it can be

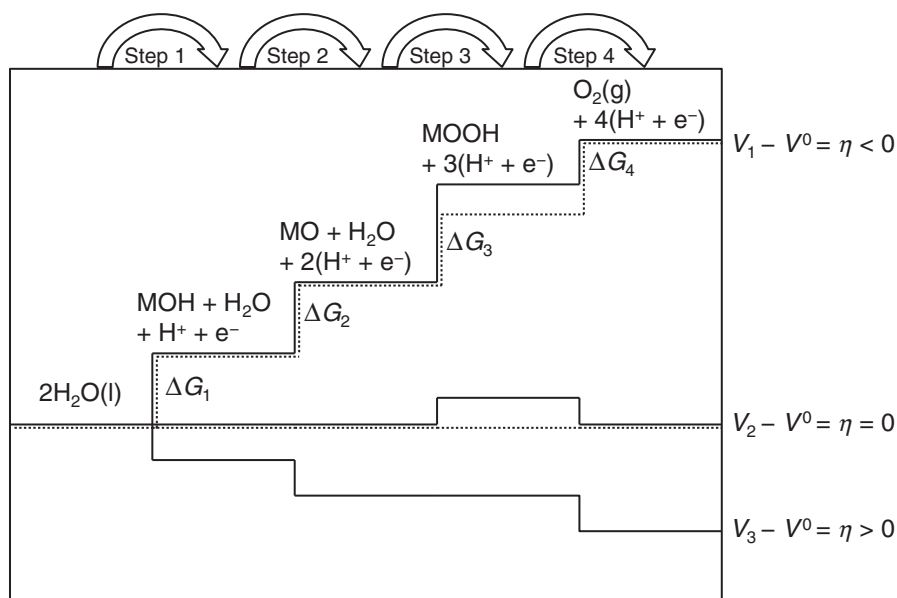


Fig. 2.5 Schematic plot of the Gibbs free energy of the reactive species and intermediates in the oxygen evolution reaction versus the reaction coordinate. *Solid lines* indicate the energetics of a ‘Real’ catalyst at three different potentials. *Dotted lines* represent the energetics of an ‘Ideal’ catalyst. Adapted from Dau et al. (2010)

seen that ΔG_3 remains positive at the reversible potential, $V_2 - V^0 = \eta = 0$. This step only becomes thermodynamically favourable when the potential $V_3 - V^0$ is reached. This potential is termed the thermodynamic overpotential as it is the potential at which all thermodynamic barriers have been removed and the overall rate of the reaction will be independent of potential (Rossmeisl 2013).

Clearly, then, the overall thermodynamics of the OER are determined by the last elementary reaction step to become thermodynamically favourable. This step is referred to as the potential-determining step (PDS) (Koper and Heering 2010), and its magnitude is simply the largest ΔG_i value such that (Rossmeisl 2013):

$$\Delta G^{\text{OER}} = \max\{\Delta G_1, \Delta G_2, \Delta G_3, \Delta G_4\} \quad (2.37)$$

In this respect, the thermodynamic overpotential is just the additional potential, past the reversible potential, required by the PDS and is given by (Rossmeisl 2013):

$$\eta^{\text{OER}} = (\Delta G^{\text{OER}}/q) - 1.23 \text{ V} \quad (2.38)$$

Importantly, this analysis allows the properties of an “ideal” catalyst to be specified. From Eq. (2.38), the optimum ΔG^{OER} value is 1.23 eV giving $\eta^{\text{OER}} = 0$. Now, since the total work to be provided by the four electrons in the OER is 4.92 eV (Rossmeisl 2013), this condition implies that $\Delta G_1 = \Delta G_2 = \Delta G_3 = \Delta G_4 = 1.23$ eV. Thus, the ideal catalyst will exhibit equally spaced adsorption energies for the OER intermediates (Rossmeisl 2013). This situation is illustrated by the “Ideal” catalyst trace in Fig. 2.5. In contrast to the “Real” catalyst, where Eq. (2.35) is the PDS, all the reaction steps become thermodynamically favourable at the same potential—the reversible potential. Furthermore, a comparison of the PDS for the “Real” catalyst with the same step in the “Ideal” case suggests that the MOOH intermediate is less stable or bound “too weakly” on the “Real” catalyst (Dau et al. 2010). Along these lines, the OER properties of the “Real” catalyst could be enhanced through stronger binding or stabilisation of the MOOH intermediate, thereby allowing the OER to proceed at a potential closer to the reversible potential. However, as will be discussed in Sect. 2.4.2, scaling relations between the free energies of related intermediates limit the effectiveness of this approach (Rossmeisl 2013).

In view of the implications for catalyst design, it is important here to distinguish between the latter concept of a potential-determining step and the kinetic concept of a rate-determining step. The approach outlined above only accounts for the thermochemistry of the elementary reaction steps, assuming that each elementary step must be thermodynamically favourable for the OER to proceed at an appreciable rate. Yet various activation barriers will also be important for the overall rate of the reaction. Indeed, the PDS and RDS need not necessarily be the same. Koper (2013) provides an instructive illustration of the significance of this distinction. Consider the two free energy plots in Fig. 2.6 for a two-step reaction involving a single intermediate. In both cases, step 1 is thermodynamically limiting with $\Delta G_1 > 0$ and so, is potential-limiting. Now, if the RDS is identified as the step that passes over

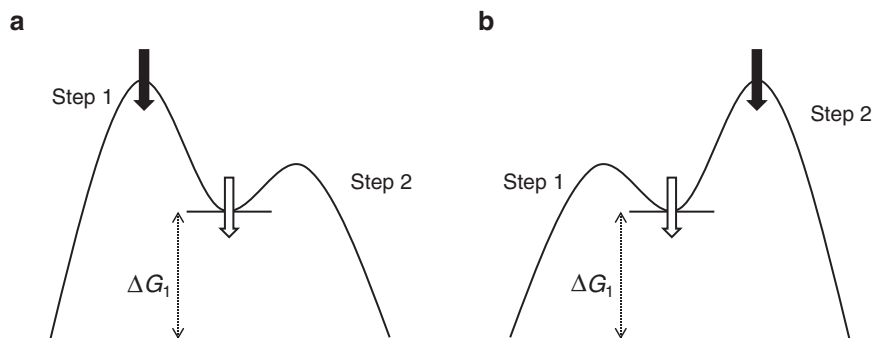


Fig. 2.6 Free energy diagrams for a two-step reaction involving a single intermediate. **(a)** Step 1 is potential determining and rate-determining. **(b)** Step 1 is potential-determining and step 2 is rate determining. Adapted from Koper (2013)

the highest energy barrier then, step 1 is rate-determining in Fig. 2.6a and step 2 is rate-determining in Fig. 2.6b. From a purely kinetic viewpoint, the rate of the reaction could be increased by facilitating the RDS. This could be achieved by lowering the energy of the transition states for step 1 and step 2, respectively, as indicated by the filled arrows in Fig. 2.6. But, if a linear relation between the activation energy and the reaction energy exists, as described by the Bronsted–Evans–Polanyi relation (Bligaard et al. 2004; Nørskov et al. 2008), then the easiest way to lower the transition states is to lower the energy of the intermediate state (Koper 2013). This approach is indicated by the unfilled arrows in Fig. 2.6. Koper (2013) notes that the real problem is not necessarily the high energies of the transition states but the high energy of the intermediate state. In this way, identifying the thermodynamically limiting step—the PDS—offers a more direct approach for catalyst design.

In this respect, it should be noted that a direct comparison between predicted thermodynamic limits and the results from electrokinetic studies is not possible, as DFT calculations do not provide overpotential values that are directly comparable with experiment (Montoya et al. 2015). Nevertheless, these interpretations are linked. Relating the PDS to the experimental observables, Rossmeisl (2013) and Rossmeisl et al. (2008) provide an expression for the kinetic current density at the anode:

$$j_a = j_0 \exp[\alpha(qV^0 - qV)/kT] = j_{\text{lim}} \exp[\alpha(qV^{\text{OER}} - qV)/kT] \quad (2.39)$$

where,

$$j_{\text{lim}} = j_0 \exp[\alpha(qV^0 - qV^{\text{OER}})/kT] \quad (2.40)$$

Here, V^{OER} is the potential at which the kinetic current is maximised and j_{lim} represents the current density achieved if all surface reactions are thermodynamically

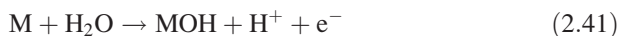
downhill, with the highest possible turn-over-frequency per site and minimal diffusion limitations. The term j_{lim} is clearly dependent on a range of factors, including the electrode structure and its interface with the liquid electrolyte, the concentration of active sites, and potential independent surface reactions. On the other hand, V^{OER} is a parameter that depends only on the catalyst material (Rossmeisl 2013). In particular, ΔG^{OER} , and therefore the thermodynamic overpotential η^{OER} , represents a lower-limit estimate of this limiting potential. Likewise, it has been noted that the experimentally observed “onset” potential for a catalytic reaction is expected to occur ca. 0.15 V prior to the predicted overpotential (Rossmeisl et al. 2008; Su et al. 2012). Taking this into consideration, Rossmeisl (2013) reaches a similar conclusion to Koper (2013) stating that differences in electrocatalytic performance between different materials are mostly described by differences in overpotentials.

2.3.2 Reaction Pathways and Surface Effects

In a strictly thermochemical description of the OER, the overall rate depends on the free energy of reaction steps involving catalyst bound intermediates. Since the energies of the reaction steps depend on the nature of the catalyst, it is important to develop a fundamental understanding of these reactions on different materials (Valdés et al. 2012). Various surface structures, types of adsorbate and solvent effects can have a strong influence on the relative stability of the reaction intermediates. Thus, the potential-determining steps and viable reaction paths can vary from one surface to another.

In their early work, Rossmeisl et al. (2007a) compared the OER activity of rutile-type oxides of RuO_2 , IrO_2 and TiO_2 . In agreement with the kinetic studies in Sect. 2.2.3, the surface coverage of intermediates was shown to be a significant factor in determining the activity of these surfaces. The authors compared the activity and stability of two different surface conditions: one surface with all bridge and coordinately unsaturated (CUS) sites occupied by oxygen (O) and one surface with these sites occupied by hydroxyl groups (OH). It was found that the O-covered surface showed the highest activity. In the case of RuO_2 , an OER overpotential of 0.37 V was predicted for the O-covered surface, whereas the HO-covered surface needed an overpotential of 0.50 V for the OER to become thermodynamically downhill. Interestingly, these limiting potentials did not correspond to the same PDS. On the O-covered surface the formation of the MOOH intermediate Eq. (2.35) was associated with the largest free energy change. But on the HO-covered surface the MO intermediate was the least stable, emphasising the influence of the local environment on the overall energy profile. Accordingly, it was suggested that hydrogen bonds between the hydroxyl groups on the HO-covered surface stabilised the MOH and MOOH intermediates relative to the MO intermediate. In any case, the O-covered surface was found to be the most stable surface at the potentials required for the OER to proceed and a comparison of the three materials under these conditions showed an activity trend of $\text{RuO}_2 > \text{IrO}_2 \gg \text{TiO}_2$.

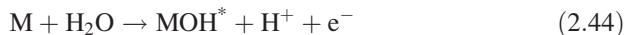
This type of analysis has since been extended to describe the thermodynamics of the OER at a range of well-defined planar oxide surfaces, including rutile, perovskite, spinel, rock salt and bixbyite oxides (Valdés et al. 2008, 2012; Man et al. 2011). Taking into account the self-consistent surface for each oxide, that is the surface that is thermodynamically stable at the necessary reaction overpotential (Su et al. 2012), the nature of the PDS is shown to be largely dependent on the oxygen binding energy at each surface (Valdés et al. 2012). On surfaces that bind oxygen strongly, the PDS is the formation of the MOOH intermediate. This is easily understood from a chemical bonding point of view; this is the O – O bond formation step and therefore, involves a reduction in the oxygen bond order with the surface. Hence, strong binding of oxygen to the surface will significantly increase the difficulty of this step. Correspondingly, for weak oxygen binding, the formation of the MO intermediate, which involves an increase in the oxygen bond order to the surface, becomes potential-limiting. It should be noted that with this transition in the PDS other reaction mechanisms become possible. This point is illustrated by the case of rutile MnO₂ (Su et al. 2012). It was found that β-MnO₂ exhibited intermediate oxygen binding energies, close to the transition point, with the result that the formation of the MO intermediate was slightly more potential-limiting than the formation of MOOH. In this case, a direct O₂ recombination mechanism was proposed:



This mechanism was found to be slightly lower in free energy by 0.08 eV than the associative mechanism in Eqs. (2.33)–(2.36). However, Rossmeisl (2013) notes that the use of alternative reaction mechanisms does not change the analysis of the PDS. It can be seen that both pathways begin with the same two steps: water splitting on the active site followed by MOH oxidation to MO. But for the direct recombination mechanism to be relevant, the free energy of oxygen binding on the surface has to be close to the free energy of oxygen in the gas phase (Valdés et al. 2012). This can only be the case for weak oxygen binding, essentially when Eq. (2.43) is thermodynamically downhill and will play no major role in the reaction kinetics. Under these conditions both mechanisms predict the same PDS, (Eq. (2.34)) or (Eq. (2.42)). Thus, for determining the overpotential to a good approximation, Rossmeisl (2013) argues that only the associative mechanism needs to be considered even though the actual reaction path might not involve MOOH formation at all.

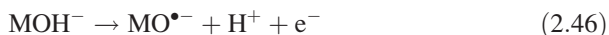
Interestingly, the self-consistent surfaces for the range of oxides considered in the latter studies were all quite similar. At the high potentials required to drive the OER, the thermodynamically most stable surfaces were those covered by oxygen

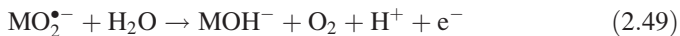
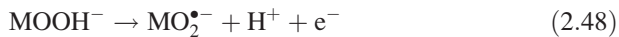
(Valdés et al 2012). Based on this result, Rossmeisl et al. (2007a) note that the interactions between water and the adsorbed reaction intermediates can be neglected, as there are no active sites available for water adsorption. However, the influence of the hydrogen bonding network surrounding such intermediates can be significant (Tuckerman et al. 1995; Marx et al. 1999; Vassilev et al. 2002). Molecular dynamic (MD) simulations of surface adsorbed hydroxyl groups indicate that the hydrogen bonding surrounding these surface bound OH species is perturbed from that of a surface water molecule (Vassilev et al. 2002). Specifically, it is shown that the oxygen-oxygen distances in the MOH hydrogen bonded complex are shorter than for water molecules in the extended network. As a result, the rate-limiting step for OH migration on a surface is the rearrangement of the local oxygen environment and not the proton transfer event itself (Tuckerman et al. 1995; Marx et al. 1999; Vassilev et al. 2002). In this way, the initial discharge of water/hydroxide at the surface could be viewed analogously as an electron transfer facilitated migration of OH^- from solution onto the surface, with a fast initial discharge step and a slow hydrogen bonding restructuring process as follows:



where MOH^* represents a higher energy surface bound hydroxyl group and Eq. (2.45) depicts the restructuring process to accommodate this energetically inequivalent species. This type of process has recently been invoked to account for the kinetic parameters observed for an IrO_2 catalyst in acidic media (Doyle et al. 2013). When the purely chemical step in Eq. (2.44) is rate limiting, a Tafel slope of 60 mV dec^{-1} and a reaction order $m_{\text{H}^+} = -1$ are predicted, in excellent agreement with experimental results (Lyons and Floquet 2011).

With this in mind, Muckerman's group have combined DFT calculations with MD simulations to explicitly account for solvation interactions at GaN, ZnO and GaN/ZnO alloy surfaces (Shen et al. 2010; Akimov et al. 2013; Kharche et al. 2014). The aqueous interface chemistry was found to profoundly affect the structure of water molecules in contact with the surface and hence, the mechanism of the OER (Shen et al. 2010; Akimov et al. 2013). Water adsorption is primarily dissociative on these surfaces such that surface anions, located at N or O sites, act as bases accepting protons from dissociated water molecules while the corresponding hydroxide ions bond with surface cations, Ga or Zn. This acid-base chemistry results in a substantially hydroxylated surface (Kharche et al. 2014) and it is at these sites that the molecular transformations involved in the OER are thought to take place (Shen et al. 2010; Akimov et al. 2013). Accordingly, the following reaction path was proposed for the OER at a GaN surface (Shen et al. 2010):





While certainly similar to the associative mechanism outlined in Eqs. (2.33)–(2.36), the distinguishing feature of this mechanism is the absence of any vacant sites. Since MD studies showed that the surface active site was unstable when vacant, the reaction is initiated at a surface attached hydroxide ion and no vacant sites are generated during the OER. This is in contrast to the associative mechanism where the OER begins and ends at a vacant surface site M. Indeed, as noted by Shen et al. (2010), it remains to be seen whether such sites would be available under more realistic experimental conditions. That said, the hydroxide oxidation step (Eq. (2.46)) is again shown to be the PDS, although in this case it represents the first step in the overall reaction.

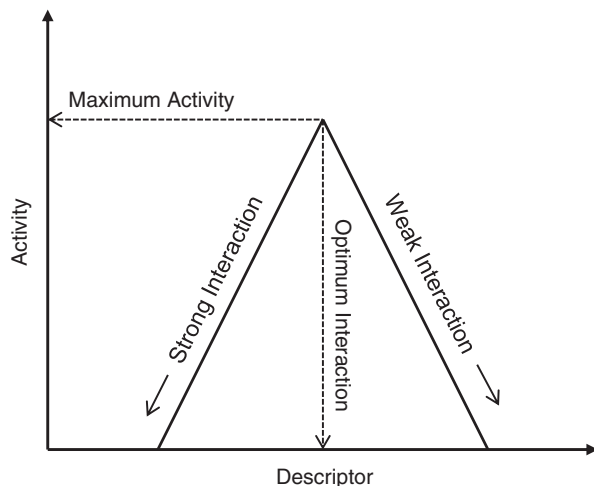
In summary, theoretical studies of the OER provide valuable insight into the microscopic properties and thermodynamic barriers associated with efficient catalysis. Though an attempt has been made here to integrate important theoretical results with experimental observations, the true power of computational studies, particularly those based on DFT, lies in their ability to describe trends in catalytic activity. In Sect. 2.4, a combined theoretical and empirical trends based analysis of the OER is discussed.

2.4 Trends in Activity

Over the past 50 years considerable research efforts have been devoted to the kinetic and mechanistic study of the OER. While significant progress has been made in terms of a theoretical understanding of the OER (see Sect. 2.3), little mechanistic consensus has been achieved. Thermodynamic and kinetic analyses of the OER are complicated by the fact that it is the metal oxide and not the metal that catalyses oxygen evolution (Conway 1995; Rossmeisl et al. 2005). These electrocatalytic materials are complex experimental systems whose catalytic activity is highly sensitive to a multitude of parameters including the surface and bulk structure of the oxide film, the manner in which the oxides are prepared and even the experimental history of the electrode (Surendranath and Nocera 2012; Doyle et al. 2013). Moreover, the way in which these properties affect the activity of electrocatalysts for the OER is not yet fully understood.

In light of this, many studies have attempted to rationalise the relative electrocatalytic activities of different electrode materials in terms of a given physicochemical property or “descriptor”. The concept of a “descriptor” involves the hypothesis that a single microscopic parameter may be a key controlling factor in a catalytic process (Dau et al. 2010; Marini et al. 2012). This hypothesis arises

Fig. 2.7 Schematic representation of a volcano plot which shows the variation in catalytic activity as a function of a reactivity descriptor. Maximum activity is achieved at an optimum descriptor value where the interaction of a key intermediate with the surface is neither too strong nor too weak



from the observation that the rate of a heterogeneous reaction shows a maximum when considered as a function of the reactivity of the catalytic surface (Sabatier 1911). This type of plot, known as a volcano plot, has been widely applied in the study of heterogeneous chemical catalysis (Dumesic et al. 2008) and a schematic representation is presented in Fig. 2.7. In principle, a descriptor could be any of a number of properties of the catalyst or catalyst–reactant interaction (Koper 2013). However, the most successful descriptors generally describe the interaction between a key reaction intermediate and the catalytic surface. In this sense, the observation of a maximum in Fig. 2.7 suggests that an optimal interaction exists. This is the Sabatier principle which states that the best catalyst binds the intermediates “just right”, neither too weakly nor too strongly (Sabatier 1911; Dumesic et al. 2008). If the interaction is too weak, the catalyst fails to activate the reactant whereas if the interaction is too strong, the surface can become blocked by intermediates or product which fails to dissociate. Thus, the identification of suitable descriptors provides knowledge of the intrinsic factors governing the experimental behaviour. This approach is particularly attractive as it lays the basis for possible predictions of catalytic activity and enables meaningful catalyst comparisons across a range of materials. In this section, the details and implications of some of the most important examples of this approach are discussed.

2.4.1 Bulk Thermochemistry

In terms of the OER, the challenge is in quantifying what is meant by the “reactivity” of an oxide surface. Early studies examined the relationship between activity and various thermodynamic data (Ruetschi and Delahay 1955; Parsons 1958; Trasatti 1980, 1984; Bockris and Otagawa 1983, 1984). The first volcano relation

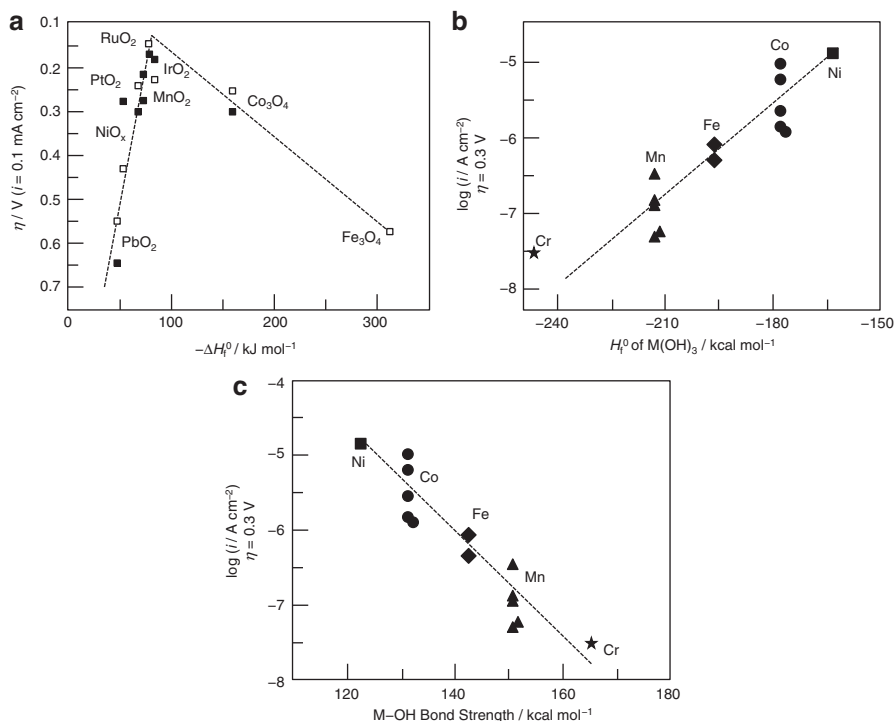


Fig. 2.8 (a) Volcano plot of OER activity for various oxide catalysts in acidic (*unfilled*) and basic (*filled*) media versus the enthalpy of a lower to higher valent oxide transition. Adapted from Trasatti (1980). (b) OER current density (based on real surface area) at an overpotential of 0.3 V for a series of perovskites versus the enthalpy of formation of the corresponding M(OH)_3 and (c) the same quantity versus the M–OH bond strength. Adapted from Bockris and Otagawa (1984) and Surendranath and Nocera (2012)

for the OER was reported by Trasatti (1980) who showed a correlation between the overpotential and the standard enthalpy change for a lower to higher valent oxide transformation, $\text{MO}_x \rightarrow \text{MO}_{x+1}$. The success of this study lies in the fact that it correctly predicted the high activity of RuO_2 and IrO_2 catalysts. As illustrated in Fig. 2.8a, the volcano plot generated for a range of binary oxides showed a peak near these state-of-the-art catalysts. This correlation can be rationalised if one considers that the OER is expected to involve one or more surface bound oxygen moieties such as MOH, MO or MOOH. The interaction of these intermediates with the surface of a given oxide MO_x could result in an increase in the coordination sphere of M, and therefore their formation would be expected to parallel the heat of formation of the oxide in the next valency state (Trasatti 1980, 1984). Along these lines, the OER can be viewed as the formation and subsequent decomposition of high-valent metal surface oxides (Dau et al. 2010).

Bockris and Otagawa (1983, 1984) found that the activity of a series of first-row transition metal perovskites (AMO_3) correlated linearly with both the standard

enthalpy of formation of the corresponding metal hydroxide $M(OH)_3$ and the metal–OH bond energy. In Fig. 2.8b, the current density at a fixed overpotential is shown to increase as the enthalpy of hydroxide formation decreases. Although a volcano peak was not observed in this case, the inverse relationship between the OER activity of perovskites and the enthalpy of $M(OH)_3$ formation suggested that the stronger the MOH bond, the weaker the catalysis. This was confirmed using calculated MOH bond energies which were also found to correlate inversely with activity, as shown in Fig. 2.8c. Interestingly, a similar trend has been observed by Subbaraman et al. (2012) who found that the oxophilicity or OH bond strength of a series of well-defined first-row transition metal hydroxide nanoclusters was a suitable descriptor for their activity. These authors showed that the OER overpotential at a fixed current density of 5 mA cm^{-2} increased in the order $Ni > Co > Fe > Mn$ indicating that the activity was inversely proportional to the OH bond strength on these catalyst surfaces. Therefore, in both cases the authors proposed that the rate of oxygen evolution was determined by the degree of difficulty in removing OH intermediates from the surface. That is, the rate determining step may be the desorption of OH or other oxygenated species from the surface, or their recombination to form the O – O bond.

2.4.2 Binding Energies and Scaling Relations

Advances in DFT calculations have enabled an explicit description of OER activity in terms of calculated adsorption energies. In Sect. 2.3.1 it was shown that OER activity is to a large extent determined by the binding strength of the reaction intermediates to the electrode surface. Depending on the number of different important surface intermediates several descriptors may be identified. For the OER at metal oxide surfaces the suggested intermediates are MOH, MO and MOOH. Indeed, subject to whichever reaction step is potential determining the binding energy of any one of these species could prove a suitable descriptor. That said, it has been shown that the binding energies of these three intermediates are strongly correlated (Rossmeisl et al. 2005, 2007a, b; Hansen et al. 2010). In general, the binding energies of intermediates which bind to a surface through the same kind of atom are found to scale linearly with each other as the electrode material is varied (Rossmeisl 2013). This point is illustrated in Fig. 2.9a, where schematic scaling relations between the binding energies of the OER intermediates and ΔG_{MOH} are presented. The slopes of these scaling relations are related to the number of bonds to the surface each intermediate partakes in. For example, the MOH and MOOH intermediates both involve a single oxygen bond to the surface and so, the slope of their scaling relation is one, whereas the slope of the scaling relation between the MOH and MO binding energies will be two, as the MO intermediate involves two bonds with the surface. Significantly, it has been found that ΔG_{MOH} and ΔG_{MOOH} are further related to each other by a constant of approximately 3.2 eV (Koper 2011):

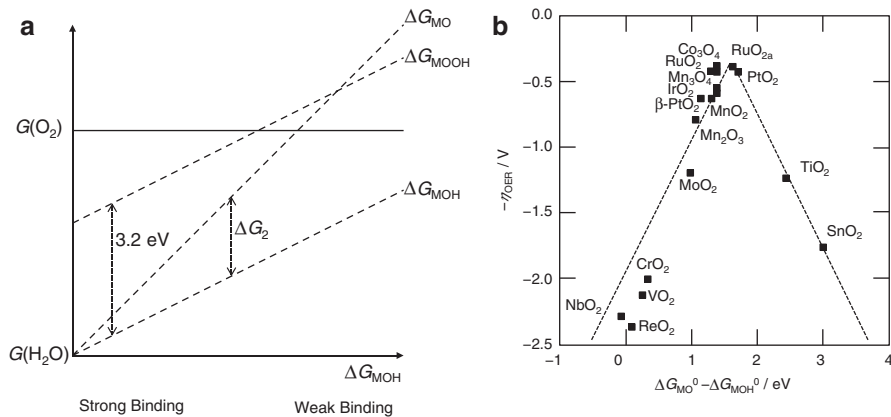


Fig. 2.9 (a) Schematic representation of the scaling relations for ΔG_{MOH} , ΔG_{MO} and ΔG_{MOOH} as functions of ΔG_{MOH} . The constant difference between ΔG_{MOH} and ΔG_{MOOH} of 3.2 eV and the universal activity descriptor ΔG_2 are also shown. Adapted from Rossmeisl (2013). (b) OER activity trends for rutile, anatase, Co_3O_4 and Mn_xO_y oxides. The negative values of the theoretical overpotential are plotted against the standard free energy difference of $\Delta G_{MO} - \Delta G_{MOH}$. Adapted from Man et al. (2011)

$$\Delta G_{MOOH} = \Delta G_{MOH} + 3.2 \text{ eV} \quad (2.50)$$

This relationship has been confirmed both for metals and for a wide range of oxide surfaces (Man et al. 2011; Koper 2011), implying that there is a universal scaling relation between the MOH and MOOH intermediates regardless of the binding site.

Taking this into consideration, the energy of the second reaction step in the associative path, ΔG_2 , has been proposed as a universal descriptor of oxygen evolving catalytic activity (Man et al. 2011). It was shown in Sect. 2.3.2 that the PDS for the OER is either the hydroxyl oxidation step (Eq. (2.34)) or the O – O bond formation step (Eq. (2.35)). Noting that the MO intermediate is involved in both steps, and taking into account the universal scaling relation, the expression:

$$\Delta G_2 = \Delta G_{MO} - \Delta G_{MOH} - qV \quad (2.51)$$

clearly contains information on the binding energies for all three important OER intermediates. Indeed this parameter has been shown to be a good general descriptor of the overpotential trends for a wide variety of oxides. In particular, it allows for a comparison between different families of oxides using a single parameter (Man et al. 2011). In Fig. 2.9b, the overpotential trends for a series of rutile, anatase, cobalt and manganese oxides are presented in a single volcano plot. Again RuO_2 and IrO_2 are positioned near the peak. Moreover, excellent agreement, in terms of trends, was found between the calculated overpotentials and the experimental results reported in the literature (Man et al. 2011).

The implications of these findings for catalyst optimisation are significant. It was shown in Sect. 2.3.1 that the ideal catalyst is defined by a free energy reaction

diagram in which the four charge transfer steps have identical reaction free energies of 1.23 eV. This can only be achieved at a specific binding of all intermediates. However, due to the scaling relations it is not possible to independently tune the binding energy of each intermediate on a surface to achieve this optimal situation. Altering the binding energy of one intermediate will also change the binding energies of all other intermediates. Moreover, the universal scaling relation between MOH and MOOH defines a lower limit estimate for the thermodynamic overpotential. Regardless of the binding energy of the MO intermediate, there is a constant difference between the binding energies of these intermediates of 3.2 eV. This is considerably more than the optimal separation of 2.46 eV, which would be expected for the transfer of two electrons and two protons, $1.23 \text{ eV} \times 2$. This discrepancy predicts a minimum overpotential of $0.37 \pm 0.20 \text{ V}$ ($=[3.20 - 2.46 \text{ eV}]/2e$) (Man et al. 2011; Koper 2011). Interestingly, as can be seen from Fig. 2.9b, the best known catalysts are already very close to this minimum value which raises the question: can OER electrocatalysis be improved? Even if the MO level can be situated optimally, half-way between the MOH and MOOH levels, within this framework there will always be an appreciable OER overpotential. This question is addressed in Sect. 2.5.1.

2.4.3 *Electronic Structure and Activity*

While the identification of descriptors has been greatly facilitated by the accurate calculation of adsorption energies, it is important to develop an understanding of the relationship between this adsorption behaviour and the fundamental properties of the catalytic material. Since the activation energies for elementary surface reactions are strongly correlated with adsorption energies (Nørskov et al. 2009), knowledge of the surface's ability to form bonds is essential. In principle, the catalytic properties of a material are completely determined by its electronic structure. In the case of pure transition metals, the “d-band” model provides a useful account of the ability of surface atoms to form bonds to an adsorbate (Nørskov et al. 2008); the higher in energy the d-states are relative to the metal Fermi level, the stronger the interaction with the adsorbate. Arising from this, the d-band centre is widely used as a descriptor for the activity of transition metals and their alloys (Mavrikakis et al. 1998; Bligaard and Nørskov 2007; Chen et al. 2008; Inoglu and Kitchin 2011). In the case of transition metal oxides, however, it is unclear whether such an interpretation can be realistically applied. The complexities of the oxide surface such as the configuration of the metal atoms and their ligands, the oxidation state of the metal and the nature of the interaction between the active site and the adsorbates, can all influence the adsorption energies (Calle-Vallejo et al. 2013). Instead, motivated by the success of d-band theory, several groups have sought a molecular level understanding of OER activity using the concepts of orbital occupancy and electron counting.

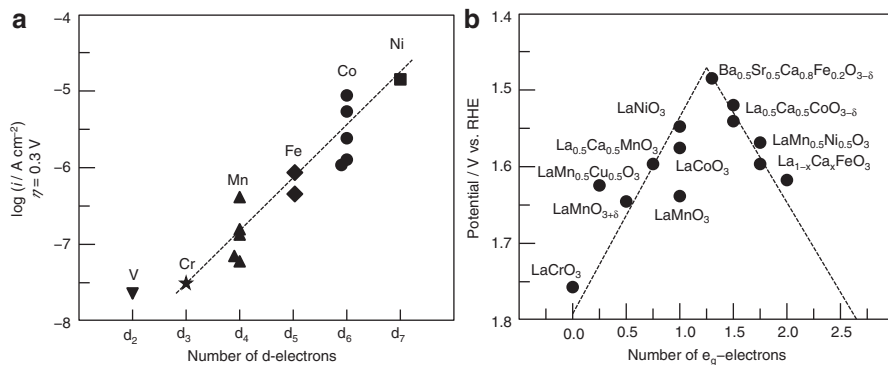


Fig. 2.10 (a) OER current density (based on real surface area) at an overpotential of 0.3 V for a series of perovskites versus the number of d-electrons of the transition metal cations. Adapted from Bockris and Otagawa (1984). (b) The relation between the OER activity, defined as the potential at 50 mA cm^{-2} of OER current, and the occupancy of the e_g -orbital of the transition metal. $x = 0, 0.25$ and 0.5 for Fe. Adapted from Suntivich et al. (2011)

In their study of the OER on perovskite oxides Bockris and Otagawa (1984) correlated the experimental trends in activity with the number of 3d-electrons of the transition metal M(III) cations. A linear increase in OER activity was observed with increasing 3d-occupancy, as shown in Fig. 2.10a. This trend is the opposite of that observed for the metal–OH bond strength in the same study, that is to say the bond strength is inversely proportional to the number of d-electrons. To account for this, these authors constructed molecular orbital diagrams for the bonding of an OH entity to an M(III)O_5 complex in an octahedral geometry. From this model of the MOH bond, they showed that the electrons from the d-orbitals of the surface transition metal in the perovskite occupy antibonding orbitals when involved in OH bonding. In this way, the decreasing bond strength was accounted for by the increasing number of d-electrons in anti-bonding orbitals. Building on this work, Suntivich et al. (2011) propose that the occupancy of a single set of molecular orbitals is a universal activity descriptor for perovskite type oxides. Noting that the octahedral splitting of the d-orbitals of atoms in the transition metal M sites results in a low energy triplet with t_{2g} symmetry and a high energy doublet with e_g symmetry, they proposed that the filling of the surface transition metal states of e_g -orbital parentage is a more appropriate descriptor for catalysis than the total number of d-electrons. This correlation is based on the idea that e_g -orbitals participate in σ -bonding with surface-anion adsorbates (Ballhausen and Gray 1962; Betley et al. 2008), and can therefore form stronger overlaps with the oxygenated adsorbates than the π -bonding t_{2g} -orbitals. Thus, the level of occupancy of the e_g -orbital at the surface transition metal site can greatly influence the binding of the OER intermediates, and consequently the OER activity. In Fig. 2.10b, the e_g -occupancy is shown to be a good descriptor of OER activity for a range of perovskite oxides. A remarkable achievement of this analysis was the prediction of the high activity catalyst $\text{Ba}_{0.5}\text{Sr}_{0.5}\text{Co}_{0.8}\text{Fe}_{0.2}\text{O}_{3-\delta}$ (BSCF). The authors found that a

near-unity occupancy of the e_g -orbital would enhance the intrinsic OER activity of perovskite transition metal oxides. Noting that BSCF had a near optimal e_g -occupancy, this catalyst was subsequently shown to have the highest experimental activity of the oxides studied (Suntivich et al. 2011).

Regardless of the approach taken, these studies show a clear correlation between OER activity and the electronic structure of the oxide. A notable study from Calle-Vallejo et al. (2013) helps to shed light on the nature of this relationship. These authors examined the relationship between the number of transition metal “outer” electrons, defined as the number of valence electrons remaining on the metal in a particular oxidation state, and the calculated adsorption energies for the OER intermediates, ΔG_{MOH} , ΔG_{MO} and ΔG_{MOOH} . Two distinct cases were considered. In the first case, the transition metal in a given type of oxide was varied in order to determine the effect of changing the number of outer electrons. In Fig. 2.11a, the trends observed for a series of monoxides are presented. The adsorption energies increased linearly with the number of outer electrons indicating a systematic weakening of the interaction. Analogous to the explanation provided by Bockris and Ottagawa (1984), this was attributed to increasing electron density in anti-bonding orbitals. The only exception was that of CaO which is easily justified as both components— Ca^{2+} and O^{2-} —have complete valence shells, making CaO inert with regard to adsorption or surface bonding (Calle-Vallejo et al. 2013). Importantly, though, it was found that the slope for ΔG_{MO} in Fig. 2.11a was twice that of both ΔG_{MOH} and ΔG_{MOOH} . This feature explains the occurrence of the adsorption scaling relations outlined in Sect. 2.4.2 and was observed for all systems examined including the pure metals as well as a range of perovskite oxides. In the second case, the oxidation state of a given transition metal was varied in order to determine the effect of changing the valence shell filling. In Fig. 2.11b, the trends observed for a range of Ni based systems are shown. Again the same linear scaling relations are present except that this time an increase in oxidation state corresponds to a weakening of the interaction. To understand this, consider a surface Ni atom coordinated to five oxygen atoms. Noting that the oxygen adsorbate completes the octahedral arrangement, the authors propose that when a Ni cation at the surface coordinates with an electrophilic ligand it must donate electrons to it in order to form the bond (Calle-Vallejo et al. 2013). In this respect, the more oxidised the metal, the fewer electrons available for bonding implying that the strength with which highly oxidised cations create bonds that require further oxidation is weak, compared with atoms of the same species in a lower oxidation state.

Taking this into consideration, the number of outer electrons is seen to be the primary electronic-structure factor influencing the surface energetics of the OER intermediates (Calle-Vallejo et al. 2013). Moreover, the fact that linear relations were observed in all cases is significant as it indicates that the number of outer electrons can be used as a descriptor to understand differences in adsorption energies not only within the same type of compound but also between different structural families. Interestingly, the number of outer electrons has also been shown to smoothly describe trends in the formation energy of various bulk oxides. Calle-Vallejo et al. (2015) showed that the formation energy for a particular oxide

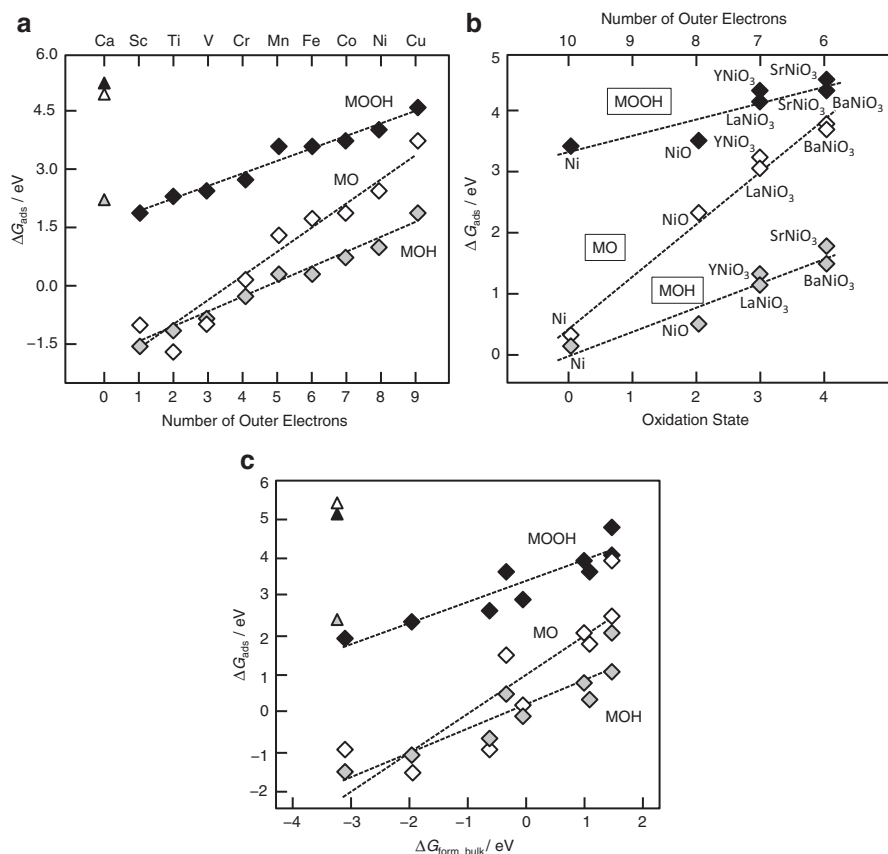


Fig. 2.11 Trends in ΔG_{MOH} , ΔG_{MO} and ΔG_{MOOH} for (a) a series of transition metal monoxides versus the number of outer electrons (b) a series of Ni compounds versus the metal oxidation state and (c) the same series of monoxides versus the bulk oxide formation energy. Adapted from Calle-Vallejo et al. (2013, 2014)

increases linearly with the number of outer electrons. By extension, the same linear scaling relations were observed between the formation energy and the adsorption energies of the OER intermediates. The corresponding trends observed for a series of first row transition metal monoxides are shown in Fig. 2.11c. This direct correlation between oxide formation energy and intermediate adsorption energy is fortuitous as it not only explains the early success of the bulk thermochemical descriptors, it validates the use of these quantities in describing OER activity trends. In fact, given the large availability of bulk thermochemical data this approach offers a simple yet chemically sound predictive model of OER catalysis.

In essence, these studies suggest that the number of valence electrons is the hidden parameter behind all successful OER descriptor models. Broadly speaking, the main driving force for the reactivity of transition metals and their oxides can be

viewed in terms of their search for maximum stability on a molecular scale (Calle-Vallejo et al. 2013). That is, the fulfilment of simple electron-counting rules by each component in the system. In this way, the varying OER activity of metal oxides can begin to be understood on a molecular level. However, while this is most certainly an important step towards a fully predictive model of catalyst design, it must be stated that any approach utilising a single parameter description of OER activity will be subject to the scaling relations outlined in Sect. 2.4.2 (Halck et al. 2014). Indeed, trends based on the number of outer electrons literally give rise to the universal scaling relations. Thus, a major challenge in OER catalysis is to find a way to modify oxide surfaces such that these design limitations can be broken, enabling the independent optimisation of the reaction parameters. In Sect. 2.5, significant developments in OER catalyst design are discussed with a view towards enhancing catalytic activity and gaining atomic level insight into the nature of the active site.

2.5 Tailoring Activity

The goal in OER catalyst development is to have enough knowledge of the factors determining catalytic activity to be able to tailor catalysts atom-by-atom (Nørskov et al. 2009). In this respect, the single descriptor models detailed in Sect. 2.4 represent an important step forward, bringing simplicity and generality to the search for improved catalysts. Yet it can be argued that this simplicity imposes artificial restrictions on catalyst design. Breaking the adsorption scaling relations on well-defined planar oxides requires a three dimensional description of activity (Halck et al. 2014)—a situation that is likely already present in real high surface area catalyst systems. Nevertheless, OER catalyst design is a complex endeavour. Prospective catalysts must not only possess high activities, but should also be electronically conductive and exhibit long term stability under the harsh operating conditions of an electrolyser unit (Chang et al. 2014). In this section, several multi-parameter frameworks to develop new catalysts with enhanced OER properties are presented. These studies provide fundamental insight into the reactivity of the oxide surface at the atomic scale—yielding useful design principles. Moreover, a significant challenge in electrocatalyst development is the identification of the catalytically active species on the catalytic surface. This section then concludes with a molecular level consideration of the nature of the active site.

2.5.1 Catalyst Synergy

Multi-component catalyst systems are one of the most promising avenues of research for OER catalyst enhancement. Various mixed oxides, dopants and catalyst substrates have been examined with a view towards garnering synergistic effects. In many cases significant improvements in catalytic activity have been observed. The beneficial effect of Fe impurities on the OER activity of Ni

hydroxides was reported over 25 years ago (Desilvestro et al. 1986; Corrigan 1987; Corrigan et al. 1987) and since then Ni–Fe based oxide catalysts have been shown to be some of the most active catalysts in alkaline media (Landon et al. 2012; Trotochaud et al. 2012; McCrory et al. 2013; Gong et al. 2013; Smith et al. 2013a, b; Louie and Bell 2013; Kim and Choi 2014). Notably, $\text{Ni}_{0.9}\text{Fe}_{0.1}\text{OOH}$ was found to have an OER turnover frequency greater than tenfold higher than that of IrO_x catalysts (Trotochaud et al. 2012). Similarly, the activity of manganese (El-Deab et al. 2007; Mohammad et al. 2008; Gorlin et al. 2014), cobalt (Yeo and Bell 2011; Lu et al. 2014) and nickel (Yeo and Bell 2012) based oxides towards oxygen evolution can be drastically increased in the presence of gold. Impurity doping in semiconductor electrodes has also been shown to lead to activity enhancements. For example, improvements in the activity of hematite (Liao et al. 2012) and rutile TiO_2 (García-Mota et al. 2011) can be observed with Ni/Co and Mn/Mo doping, respectively. Even in the case of state-of-the-art ruthenium oxide based catalysts significant increases in OER activity have been obtained by mixing with Ni or Co (Pettrykin et al. 2010).

In an effort to better understand this catalytic enhancement, several models have emerged describing the reactivity of these catalysts at the atomic scale. Halck et al. (2014) proposed a hydrogen acceptor model to account for the enhanced OER activity of Ni and Co modified RuO_2 . This model assumes an associative reaction pathway (Eqs. (2.33)–(2.36)) and suggests a stabilisation of the MOOH intermediate through localised hydrogen bonding or full proton transfer. A schematic representation of this model is presented in Fig. 2.12. For rutile type oxide catalysts, the OER is thought to occur on the surface CUS sites, as these sites provide reactive “atop” positions essential for the formation of strongly adsorbed intermediates (Halck et al. 2014). In the hydrogen acceptor model, it is envisaged that the local CUS site architecture is modified by the incorporation of the heterovalent Ni/Co cations. The oxygen bridge positions, which are generally considered to be inactive, get activated by the presence of the nearby Ni or Co such that the bridging O accepts a strong hydrogen bond or even adsorbs the hydrogen from the MOH and MOOH intermediates, as shown in Fig. 2.12. This results in a significant deviation in the overall energetics of the OER from the conventional analysis outlined in Sect. 2.3. In Fig. 2.12 it can be seen that the free energy changes for step 1 and step 3 on the Ni and Co modified RuO_2 are lowered compared with those on pure RuO_2 , but not by equal amounts. This is an important observation as it indicates that the universal scaling relation between the binding energies of the MOH and MOOH intermediates no longer applies. That is, the thermodynamic limitation of the overpotential to ca. 0.37 V has been removed and the OER can proceed at potentials closer to the reversible potential. Accordingly it was found that the largest reaction energies for the Ni and Co modified RuO_2 were 1.49 eV (step 2 potential-determining) and 1.33 eV (step 1 potential-determining) respectively, which gave rise to corresponding thermodynamic overpotentials of ca. 0.26 and 0.1 V. This trend was confirmed experimentally where a series of $\text{Ru}_x\text{Ni}_{1-x}\text{O}_2$ and $\text{Ru}_x\text{Co}_{1-x}\text{O}_2$ catalysts were all shown to outperform the pure RuO_2 catalyst (Halck et al. 2014).

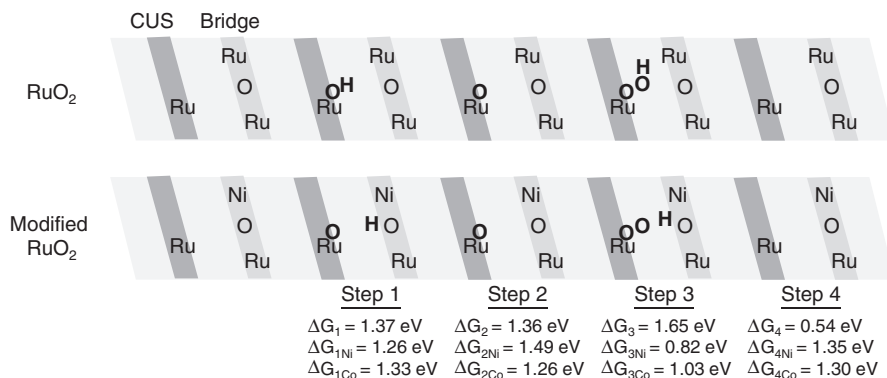


Fig. 2.12 Schematic representation of the reaction mechanism for the oxygen evolution reaction on conventional rutile RuO_2 and Ni/Co modified RuO_2 illustrating the role of the two binding sites. The *dark grey* row represents the CUS sites and the *lighter grey* the bridge sites. Adsorbed intermediates are represented in **bold font**. The Gibbs free energies obtained from DFT calculations for each of the reaction steps are included. Adapted from Halck et al. (2014)

In this way, decoupling of the MOOH and MOH binding energies makes it possible to tune the catalytic properties of a material by varying the hydrogen acceptor. Indeed, Halck et al. (2014) have successfully extended this analysis to model the beneficial interaction of both Mn and Co with gold. Various literature reports have highlighted significant improvements in OER activity when Au is added to Mn or Co based catalysts. For example, El-Deab et al. (2007) and Mohammad et al. (2008) compared the OER electrocatalytic activity of $\gamma\text{-MnOOH}$ nanorods deposited on Au, Pt and glassy carbon substrates. They found that the lowest overpotential, by more than 200 mV, was obtained for a manganese oxide modified Au substrate. Similarly, it has been shown that the OER turnover frequency, measured at an overpotential of 400 mV, for MnO_x nanoparticles is increased 20-fold when they are co-deposited with Au nanoparticles (Gorlin et al. 2014). Likewise, gold nanoparticles have also been found to enhance the OER activity of mesoporous Co_3O_4 (Lu et al. 2014). Applying the hydrogen acceptor model, Frydendal et al. (2015) suggest that $\text{Au}=\text{O}$ functionalities on the gold nanoparticles/substrates act to lower the energy of the MOOH intermediate in the same way as the rutile oxygen bridge sites. The inclusion of this gold hydrogen acceptor in the theoretical analysis predicted a lowering of the thermodynamic overpotential for several Mn and Co based catalysts by ca. 0.1–0.3 V, in line with the experimental observations (El-Deab et al. 2007; Mohammad et al. 2008; Gorlin et al. 2014; Lu et al. 2014). Thus, the addition of a proton donor-acceptor functionality represents a simple multi-dimensional approach for the optimisation of the electrocatalytic surface.

Busch et al. (2011a, b, 2013a, b) provide an alternative interpretation of the origin of such catalytic enhancement, arguing that mixing transition metal oxides with opposite reactivity can lead to improved catalytic performance. In contrast to

the hydrogen acceptor model, these authors assumed a binuclear reaction path similar to the Bockris Electrochemical Oxide (Table 2.1)/direct recombination mechanism (Eqs. (2.41)–(2.43)). The potential catalytic performance of a series of homo-(bi)nuclear transition metal catalysts was evaluated with respect to the two primary steps in the mechanism: the oxidation of two MOH hydroxyl groups to form two MO oxo groups and the subsequent μ -peroxo bond formation between the MO groups. The choice of transition metal was shown to have a significant effect on the stabilities of the MO intermediates. In particular, two distinct classes of compound were identified depending on the degree of single bond character in the $M = O$ bond of the MO intermediate (Busch et al. 2011a, 2013a). The energetics of these two classes are typified by the Fe–Fe and Co–Co reaction energy diagrams in Fig. 2.13. For the Co–Co (Mn–Mn, Ni–Ni) catalyst the MO moieties contain considerable radical character and so, their formation is endothermic requiring an overpotential of approximately 0.5 eV (1.06 eV/2) relative to a tyrosine reference potential.⁴ As a result, the subsequent O–O bond formation becomes strongly exothermic of the order of -0.75 eV. On the other hand, the $M = O$ bonds are stable for the Fe–Fe (Cr–Cr, V–V) catalyst with the result that the two MOH oxidation steps are exothermic. This stabilisation leads to an O–O bond formation step that is strongly endothermic of the order of 0.75 eV. In both cases, it is clear that significant overpotential or thermal activation is necessary for the reaction to proceed. Based on these findings, Busch et al. (2011b) proposed a hetero-nuclear Fe–Co catalyst as an attractive compromise which could overcome the shortcomings of the individual homonuclear catalysts. While this catalyst can follow two pathways—forming Fe=O or Co=O first—it can be seen from Fig. 2.13 that the inertness of Fe=O was counteracted by the reactivity of the Co=O to the extent that the di-hydroxo species displays a negligible endothermicity or overpotential of 0.11 eV and the μ -peroxo formation step is slightly exothermic by -0.14 eV. This finding is consistent with experimental observations that the OER performance of Fe₃O₄ based catalysts can be improved by combining with Mn and Co oxides (Singh et al. 1996; Rios et al. 1999; Merrill and Dougherty 2008; McCrory et al. 2013). Therefore, by mixing oxides from opposing reactivity groups it may be possible to selectively tune the relative energies of important intermediates, leading to minimal OER reaction barriers.

On the other hand, several authors have attributed the catalytic enhancement to changes in the local electronic properties of the active sites. Yeo and Bell (2011, 2012) compared the OER activity of Ni and Co oxides prepared on a range of substrates. They observed that the OER activity of a submonolayer of cobalt oxide decreased with decreasing electronegativity of the substrate in the order $\text{CoO}_x/\text{Au} > \text{CoO}_x/\text{Pt} > \text{CoO}_x/\text{Pd} > \text{CoO}_x/\text{Cu} > \text{CoO}_x/\text{Co}$ (Yeo and Bell 2011). Similarly, it was found that a monolayer of nickel oxide deposited on Au exhibited greater electrocatalytic activity when compared with an equivalent layer deposited

⁴The significance of this reference potential is beyond the scope of this discussion but interested readers are directed to Busch et al. (2011a, 2011b) for more details.

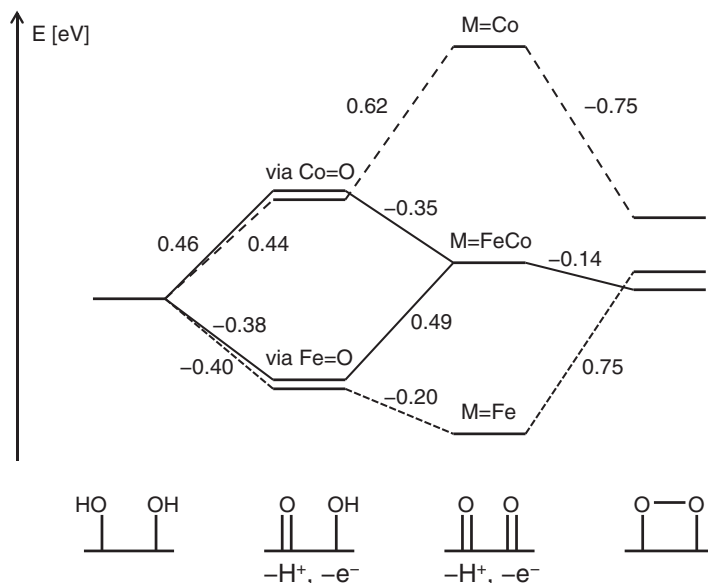


Fig. 2.13 The reaction energetics for hydroxide oxidation and μ -peroxo bridge formation at the homo-binuclear Fe (*short dash*) and Co (*long dash*) sites and hetero-binuclear FeCo (*solid lines*) sites showing the step-by-step dehydrogenation processes. All energy values are given in eV. Adapted from Busch et al. (2011a, b)

on a Pd substrate (Yeo and Bell 2012). In all cases the increase in activity follows the trend in electronegativities and may be the result of partial electron transfer from the oxide to the more electronegative metal substrate. This concept has been elaborated on by Trotochaud et al. (2014) to account for the extraordinary synergy in Ni-Fe based catalysts. It has been shown that the Fe in these catalysts is predominantly found in the Fe^{3+} oxidation state (Corrigan et al. 1987; Kim et al. 1994; Balasubramanian et al. 2000). However, at potentials associated with active oxygen evolution, V -pH (Pourbaix) diagrams predict that both Fe^{3+} and Fe^{4+} could be stable (Pourbaix 1974; Schweitzer and Pesterfield 2010). In principle, partial-charge transfer can therefore occur between the Fe and Ni centres. For example, Corrigan et al. (1987) found evidence from in situ Mossbauer spectroscopy of partial electron transfer away from Fe^{3+} centres when Ni^{3+} centres were further oxidised to Ni^{4+} . In addition, the potential of the $\text{Ni}^{2+}/\text{Ni}^{3+}$ redox couple has been shown to depend on the Fe content of the film (Louie and Bell 2013; Trotochaud et al. 2014). The presence of Fe effectively makes it more difficult to oxidise Ni^{2+} . Based on these observations, Trotochaud et al. (2014) suggest that partial electron transfer between the Ni and Fe centres leads to Ni^{3+} or Ni^{4+} species with more oxidising power and thus, enhanced OER activity. In this way, altering the electrophilicity of the active centres, through the relative electronegativities of the component metals, represents an experimentally facile approach to catalyst optimisation.

2.5.2 Activity–Stability Relations

The requirement of long-term stability for an OER catalyst is clear and widely acknowledged (Merrill and Dougherty 2008; McCrory et al. 2013; Fabbri et al. 2014). Even if it could be born economically, the frequent replacement of electrode materials makes little sense from both an operational and energy supply standpoint. However, a key question that is rarely addressed is: What is the relationship between the stability of an oxide material and its activity for the OER? While this relationship is addressed implicitly in the volcano relations detailed in Sect. 2.4—simply put, the most active catalyst is neither too reactive nor too stable—an explicit understanding of the atomic scale stability of oxide materials during the OER is lacking.

The potential impact of such knowledge on the development of OER catalysts is highlighted by the work of Markovic’s group (Chang et al. 2014, 2015; Danilovic et al. 2014b). These authors studied the fundamental links between the activity and stability of well-defined monometallic and bimetallic oxides, arguing that it is the stability, or lack thereof, of surface atoms that controls the OER activity of oxide materials. In these studies, the activity of a particular oxide was given by the overpotential measured at 5 mA cm^{-2} of OER current density and the stability of each oxide was defined by its degree of dissolution, as quantified by the concentration of corresponding metal ions in solution following each OER polarisation experiment. The trends observed for a series of monometallic oxides in acidic media are presented in Fig. 2.14. In order to discern any structural effects, two types of oxide with very different morphologies were examined: for each metal a crystalline thermally prepared oxide (TC) and a highly defective amorphous electrochemically prepared oxide (EC) were studied. It can be seen from Fig. 2.14 that the OER activity of both types of oxide increased with the oxophilicity of the metal in the order $\text{Os} \gg \text{Ru} > \text{Ir} > \text{Pt} > \text{Au}$ and that the activity was inversely proportional to the stability of the oxide. Notably, Os was found to be considerably more active than Ru but was also extremely unstable. Furthermore, the amorphous oxides all showed higher activity but less stability than the crystalline oxides. Given the higher density of defects in the EC-oxides relative to the TC-oxides, it was noted that the density of surface defects may play a significant role in the relationships between activity and stability (Danilovic et al. 2014b). Similar trends were also observed for a range of polycrystalline and single crystalline oxides (Chang et al. 2014; Danilovic et al. 2014b). In all cases the most defective surfaces were the most active and the least stable, suggesting that the inverse relationship between activity and stability is a general phenomenon in OER electrocatalysis.

Taken together, these studies show that both the nature of the oxide and the density of surface defects play an important role in controlling the stability and reactivity of surface atoms (Chang et al. 2015). This relationship has been explained in terms of a potential induced transformation from a stable low-valence oxide into an unstable higher-valence oxide, reminiscent of the O’Grady pathway in Table 2.1. It was observed that the onset of Ru and Ir dissolution for polycrystalline surfaces

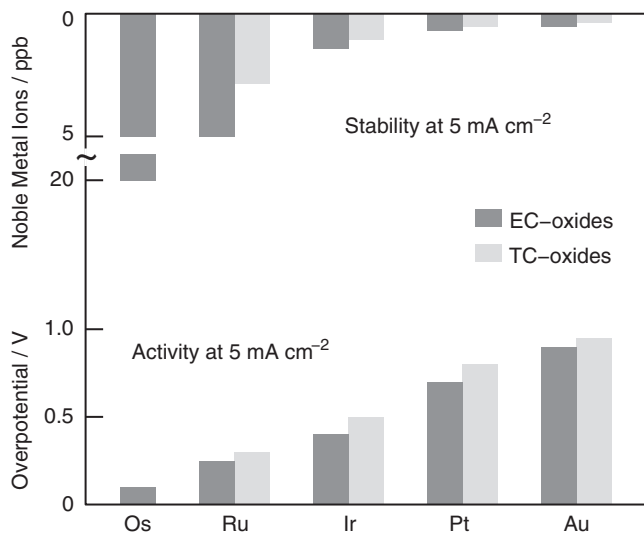


Fig. 2.14 Relationships between activity and stability for the oxygen evolution reaction on monometallic oxides. Activity: overpotential at 5 mA cm^{-2} . Stability: the concentration of dissolved metal ions in the electrolyte solution following OER polarisation up to 5 mA cm^{-2} . Adapted from Danilovic et al. (2014b)

was always accompanied by the onset of OER current density (Danilovic et al. 2014b). Using in-situ X-ray near edge structure (XANES) analysis these processes were found to coincide with a change in the average metal oxidation state from $n = 4$ to a less well-defined $n > 4$ state. Significantly, the extent to which this transition occurred mirrored the activity and stability trends. Polycrystalline Ru showed a greater rate of oxidation than polycrystalline Ir, consistent with its higher activity and lower stability. On this basis the active sites for these catalysts were identified as locations on the electrode surface where the transition from the stable $n = 4$ state to the unstable $n > 4$ state is facilitated, such as defect sites (see Sect. 2.5.4), highlighting how potential dependent variations in the oxidation state of surface atoms govern the stability of, and induce activity in, these oxides (Danilovic et al. 2014b; Chang et al. 2015).

This link between the intrinsic activity and stability of oxide materials provides an interesting interpretation of OER catalyst optimisation. In this framework, the best materials for the OER should balance activity and stability in such a way that the dissolution rate is neither too fast nor too slow (Danilovic et al. 2014a; Chang et al. 2015). This is seen clearly in the nanoscaling effects reported for Ru catalysts. Reier et al. (2012) compared the activity of bulk and nanoparticulate Ru catalysts in acidic media. While these catalysts exhibited similar activities, the Ru nanoparticles suffered from strong corrosion at the applied OER potentials and were unable to sustain their activity. Even on Au “the noblest of metals” the OER has been shown to follow a decomposition mechanism. Diaz-Morales et al. (2013) performed online mass spectrometry analysis of the oxygen evolved from

polycrystalline Au surfaces. Using ^{18}O labelling of the surface oxide, they showed that the very first oxygen evolved was $^{18}\text{O}_2$, which could only have arisen from the surface oxide layer, indicating that the initial oxygen evolution process was accompanied by decomposition of the surface oxide. In an effort to overcome these stability limitations the Markovic group have developed a new synthesis strategy that is based on the concept of surface segregation or surface enrichment (Ruban et al. 1999; Novell-Leruth et al. 2013; Danilovic et al. 2014a). Thermal annealing of $\text{Ru}_{0.5}\text{Ir}_{0.5}$ alloys and nanoparticles was shown to enrich the catalyst surface with the more stable Ir atoms (Danilovic et al. 2014a). This resulted in the formation of a nano-segregated surface domain that enhanced the stability of the catalyst four-fold without compromising its OER activity. Thus, tuning the near-surface composition of mixed oxide catalysts affords a viable strategy for balancing catalyst activity and stability.

2.5.3 Conductivity Effects

The conductivity properties of the catalyst film can strongly impact its performance as an oxygen evolution electrocatalyst. Efficient charge transport to the active site is crucial if the reaction is to proceed at a practical rate. This can be a major limitation for many metal oxides as they lack the conductivity of the parent metal (Bockris and Otagawa 1984; Matsumoto and Sato 1986). As a result, the extent to which the applied potential is translated to the oxide–electrolyte interface can vary over a large range. In cases where the catalyst film is not sufficiently conductive, a portion of the potential will drop across the catalyst film in order to drive the current transport, leading to a lower apparent activity relative to a more-conductive film (Trotochaud et al. 2014). Therefore, from the perspective of catalyst optimisation, it is important to be able to decouple these conductivity limitations from the intrinsic catalytic activity.

A number of authors have proposed a dual energy barrier model to account for conductivity limitations in thin surface oxide layers (Meyer 1960; McDonald and Conway 1962; Lyons and Brandon 2010; Doyle and Lyons 2014b). Electrokinetic studies of the OER rely on the assumption that the measured current is a direct result of the interfacial charge transfer process. However, in situations where the current is also dependent on the charge-transport efficiency through the oxide film, interpretation of the kinetic parameters can be more complicated. In this respect, the dual energy barrier model assumes that only a fraction ΔV_{FS} of the total potential difference between the metal support and the electrolyte ΔV_{MS} determines the electrochemical charge transfer kinetics in the double layer (McDonald and Conway 1962). The remainder ΔV_{MF} appears across an electronically semi-conducting “barrier” oxide, through which the charge passed must migrate under the influence of an electric field. In this way, the process can be considered equivalent to a complex electrode reaction with two rate limiting steps following one another: charge migration through the oxide film and charge transfer at the electrolyte

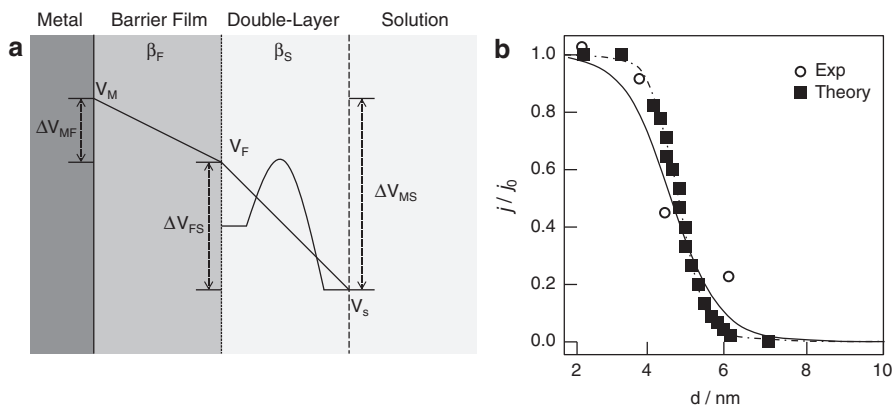


Fig. 2.15 (a) Schematic representation of the dual energy barrier model showing associated potential gradients through the barrier film and double-layer interface. Adapted from McDonald and Conway (1962). (b) Comparison of theoretical (*squares*) and experimental (*circles*) data for the oxygen evolution current density at 2.0 V vs. RHE. The current density is normalised relative to a 1.2 nm TiO₂ sample and a roughness of about 0.5 nm is included in the analysis. Adapted from Viswanathan et al (2014)

interface, as shown schematically in Fig. 2.15a. The result of this is a composite symmetry factor for the overall process across the two barriers as follows:

$$\beta_{\Sigma} = \frac{\beta_F \beta_S}{\beta_F + \beta_S} \quad (2.52)$$

where β_F is the symmetry factor for field assisted charge transport through the oxide and β_S represents the symmetry factor for the electrocatalytically rate-determining electron transfer reaction. A similar dual barrier expression can also be derived for the effective reaction order with respect to the activity of a particular reactant a_S :

$$\frac{d \log i}{d \log a_S} = \frac{m_S \beta_F}{\beta_F + \beta_S} \quad (2.53)$$

where m_S is the expected value of the reaction order in the absence of dual barrier conditions. In this way the true mechanistically significant kinetic parameters can be extracted from the overall current response. Although this model was originally suggested for monolayer Au oxides, McDonald and Conway (1962) suggest that it can be logically extended to layers thicker than a monolayer and so, should be generally applicable for thin compact oxides through which facile charge transport cannot be assumed.

In relation to this, Viswanathan et al. (2014) propose that there is a critical thickness for such compact oxide films beyond which charge-transport should always be considered. Utilising TiO₂ as a model system, these authors explored the role of coherent tunnelling as a mode of charge transport in electrocatalytic

materials with low conductivity. To account for the possibility of electron tunnelling, the equation for the kinetic current density (Eq. (2.39)) can be modified as follows (Viswanathan et al. 2014):

$$j = j \min \left(\exp \left\{ - \frac{q(V - V_{\text{bias}} - V^{\text{OER}})}{kT} \right\}, 1 \right) \left| [j_t(qV_{\text{bias}}) = j] \right. \quad (2.54)$$

Here, the tunnelling current density j_t is dependent on the potential difference across the film and must be sufficient to sustain the electrochemical current density j . This condition gives rise to a minimum potential bias V_{bias} which can have a significant influence on the observed electrocatalytic activity—appearing as an apparent increase in overpotential or a decrease in the current density at a fixed potential. For example, calculated and experimentally measured current densities at a fixed OER potential are plotted as a function of the TiO_2 layer thickness in Fig. 2.15b. For sufficiently thin films it was found that tunnelling can contribute in a dominant way to charge transport with the result that below a thickness of ca. 4 nm, V_{bias} was negligible and the OER kinetics were unchanged. However, for thicker layers, charge-transport begins to limit the OER current density. The tunnelling current density at a fixed V_{bias} was shown to decay rapidly with increasing layer thickness. Accordingly, a greater proportion of the applied potential is necessary to drive the tunnelling process resulting in a decrease in the observed OER current density as the layer thickness increases. Based on these observations the authors suggest that nanostructuring offers a potential solution; by lowering the distance required for the charge to travel and allowing for additional charge transport mechanisms such as tunnelling to become active, the intrinsic activity of the catalyst film can be studied irrespective of its bulk conductivity (Viswanathan et al. 2014).

While these studies have focussed on the electronic conductivity of compact anhydrous oxides, alternative charge transport mechanisms will become important for more porous structures. In electrochemically prepared hydrous oxides the electric field decays rapidly within a few nanometers of the electrode support (Surendranath and Nocera 2012). Redox centres immediately adjacent to the support electrode are directly affected by the electrode potential, whereas charge is further propagated along the oxy-metal strands through an electron hopping mechanism (Fachinotti et al. 2007; Lyons et al. 2011; Doyle et al. 2013). Importantly, this electron hopping process is accompanied by the transport of ions along the same path and as such, the ionic conductivity of these films can also be a key determinant of their electrocatalytic performance.⁵ However, even for these highly porous films, simple attempts at facilitating electron transport within the film, such as the incorporation of conductive carbon architectures, have yielded significant

⁵ IS and CV studies can provide a useful qualitative and quantitative characterisation of the charge-transport processes in mixed ionic/electronic conductors. The IS analysis of such processes is discussed in detail by Bisquert et al. (2000a, 2000b) and Terezo et al. (2001), whereas the CV characteristics have been comprehensively reviewed by Doyle et al. (2013).

catalytic enhancements. An electrochemically prepared hydrous Fe oxide/single walled carbon nanotube composite catalyst showed a 50 mV reduction in OER overpotential relative to the pure hydrous oxide, with a three-fold increase in turnover frequency (Doyle and Lyons 2014a). This enhancement was attributed to the superior conductivity of the composite film—IS analysis of the film during active oxygen evolution showed an eight-fold decrease in charge transfer resistance compared with the pure hydrous oxide film. Similar enhancements in catalytic activity have been reported for a range of chemically synthesised spinel oxide/graphene composite catalysts including Co_3O_4 (Liang et al. 2011), MnCo_2O_4 (Wang et al. 2011; Liang et al. 2012), NiCo_2O_4 (Lee et al. 2013) and CoFe_2O_4 (Bian et al. 2014).

Additionally, nanostructuring has also been shown to enhance the activity of amorphous electrodeposited oxides, although in this case it appears that increasing rather than decreasing the charge transport network is necessary. This is illustrated clearly for the cobalt catalyst films developed by Nocera's group (Farrow et al. 2013). Catalyst films formed in borate (CoBi) and phosphate (CoPi) electrolytes showed marked differences in activity with increasing film thickness. In both cases the performance of the layer increased with thickness reflecting an increase in effective surface area, as would be expected for a porous layer. However, whereas the CoBi films displayed a monotonic increase in activity with film thickness, the activity of CoPi reached a limiting activity. This observation correlated with structural differences in the catalyst films: CoBi films exhibited coherent domains consisting of 3–4 nm cobaltate clusters (see Sect. 2.5.4) with up to three layers, whereas CoPi films comprised significantly smaller clusters that were not coherently stacked. It was suggested that the larger domain size and lower disorder of CoBi relative to CoPi facilitated intralayer and interlayer hopping of electrons, providing for greater charge transport mobility in the CoBi films. In this way the effective concentration of catalytic sites could be more easily increased for the CoBi films while still maintaining an efficient charge transport network. Thus, an effective OER catalyst design protocol should also include the careful engineering of the material structure, so that conductivity can be maximised while preserving the surface structures necessary for efficient catalysis. In Sect. 2.5.4 the specific nature of these catalytically active surface structures is discussed.

2.5.4 The Active Site

It is generally accepted that surface reactions occur predominantly at active sites (Schwab 1981; Burke et al. 2000, 2003). This concept, first introduced almost a century ago by Taylor (1925), is based on the idea that heterogeneous reactions do not take place over the entire available catalytic surface but are instead localised at specific catalytically active surface sites. Although pinpointing these active sites experimentally has proven difficult, some consensus has been achieved regarding their general properties. In the case of metal and metal oxide surfaces, the active

sites are thought to be located at surface defects in the lattice structure. Somorjai (1996) pointed out that, for the same surface, catalytic processes occur much more rapidly at defects, such as kinks and ledges, than on terraces, stressing that more defective surfaces are most active—a point supported by the work of Markovic's group discussed in Sect. 2.5.2. Similarly, Sun et al. (2012) found, using a combined Hückel theory and DFT approach, that the most thermodynamically stable oxygen adsorption sites on Au are those with the potential for multi-fold coordination. Moreover, Nowicka et al. (2010) have shown that the active sites on Au can be selectively “knocked out” by treatment with hydroxyl radicals, suggesting that surface defects are the loci of partially filled d-orbitals that can stabilise free-radical intermediates. From these observations it seems clear that sites with low lattice coordination at the atomic level control the surface reactivity. However, the specific nature of these sites is still not well understood, hence the somewhat ambiguous representation of the OER active sites by M in this work. A fundamental challenge in OER catalyst design is understanding the processes occurring at these sites at the microscopic level.

An intuitively chemical description of OER catalysis has been provided by the groups of Burke and Lyons (Burke and O'Sullivan 1981; Lyons and Burke 1987; O'Sullivan and Burke 1990; Rebouillat et al. 2011; Lyons et al. 2011; Doyle et al. 2013). These authors contend that the specific nature of the active site can be envisaged if attention is paid to the underlying surface redox chemistry of the oxide. In aqueous solution, metal oxide surfaces have a significant hydrophilic character with the result that surface oxy groups can become extensively hydrated or hydroxylated (Burke et al. 1982b; Egdell et al. 1983). For compact crystalline oxides this hydration is likely restricted to coordinately unsaturated surface defect sites, whereas for more porous oxides the hydration can permeate deeper into the layer. Indeed, for anodically generated hydrous oxide films it appears that the oxy-metal cations are hydrated at the individual level, virtually intermingling with the solution phase (Burke and Lyons 1986). In this way, it is suggested that metal oxides share a common surface–electrolyte interface, only differing in the extent of their hydration/hydroxylation, as illustrated in Fig. 2.16. Importantly, insight into the structure of these hydrated surface species is afforded by an examination of their distinctive redox behaviour. Negative *super-Nernstian* V -pH shifts have been observed for the redox transitions of a number of transition metal oxide surfaces including Ni (Burke and Twomey 1984; Lyons et al. 2012a, b) Fe (Burke and O'Sullivan 1978; Burke and Lyons 1986; Doyle and Lyons 2013a, b) Au (Burke et al. 1982b) Rh (Burke et al. 1981) Ir (Burke and Whelan 1984) and Ru (Lyons and Burke 1987; Lyons and Floquet 2011) implying that the oxidised state of these oxides acquires a net negative charge relative to the reduced state. This anionic oxide formation arises from well-known hydrolysis reactions which accompany the oxidation of the metal cations (Burke and Lyons 1986; Sato 1998), and can be equivalently regarded in terms of the adsorption of excess OH^- ions, proton loss from coordinated water molecules or the formation of hydroxyl surface complexes. Based on these considerations, a general structure for the hydrated surface species

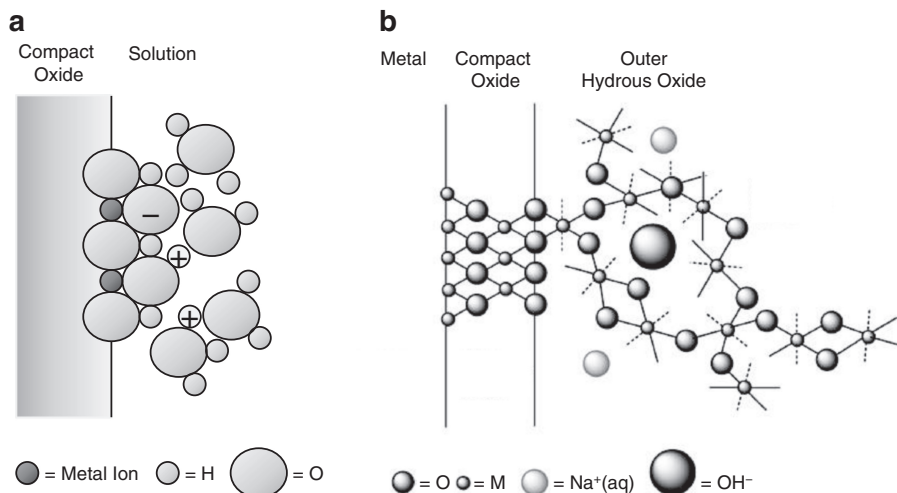
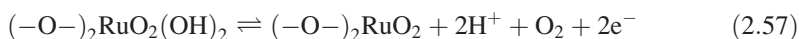
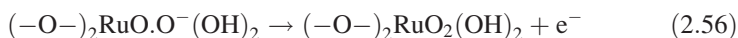
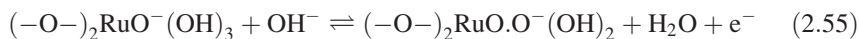
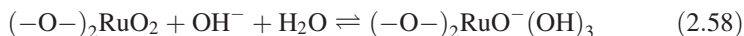


Fig. 2.16 Schematic representation of the oxide-solution interface for (a) compact thermally prepared oxides such as RuO₂ and (b) anodically prepared hydrous oxides. In both cases the electrocatalytically active region is hydrated containing octahedrally co-ordinated surfaquo groups either individually dispersed or interlinked in a more extended network. Adapted from Lyons et al. (2014)

has been proposed: $\left[M(z)O_m(OH)_n(OH_2)_y \right]^{p-}$ where $p = 2m + n - z$ and z is the oxidation state of the metal M , which should apply to any oxide phase known to acquire a net negative charge in aqueous solution. Accordingly, the electrocatalytic activity of the various oxide films can be ascribed to the presence of complex anionic surface clusters, consisting of octahedrally co-ordinated metal complexes—the *surfaquo* group.

It is important to emphasise here that the formulae for these anionic species are devices presented to rationalise the observed V -pH behaviour; the exact surface stoichiometry is often unknown and will depend on the nature of the metal cation and its energetically stable coordination states. However, it is believed that this chemically intuitive approach is more realistic than thinking in terms of discrete stoichiometric oxide species. In their original work on thermally prepared Ru based oxides, Lyons and Burke (1987) proposed that the OER took place at Ru surfaquo groups according to the following reaction sequence:





Here the surfaquo groups are linked to the oxide surface by two bridging oxygen species ($-O-$). With the second electron transfer step being rate-determining, this mechanism was shown to be in good agreement with the observed electrokinetic data: $b = 60 \text{ mV dec}^{-1}$ and $m_{OH^-} = 1$. Building on this concept, surfaquo groups have been specifically implicated as the OER catalytic centres on several thermal oxide (Lyons and Burke 1987; Lyons and Floquet 2011; Godwin et al. 2014), passive oxide (Lyons and Brandon 2010; Doyle and Lyons 2014b) and hydrous oxide surfaces (O'Sullivan and Burke 1990; Lyons and Brandon 2009; Lyons et al. 2012a, b; Doyle and Lyons 2013a, b). In particular, the pH dependence of the OER on hydrous Fe oxides was shown to mirror that of the surface redox processes, as shown in the inset of Fig. 2.17 (Doyle and Lyons 2013a, b). Rather than the expected V -pH shift of -59 mV/pH unit for a process involving equivalent proton/hydroxide and electron transfer, the OER onset potential exhibited a -93 mV/pH super-Nernstian shift of similar magnitude to the primary hydrous oxide redox transition A3. On this basis it was suggested that the anionic surfaquo groups located throughout the hydrous layer actively partake in oxygen evolution, and the mechanism outlined in Fig. 2.17 was shown to be in excellent agreement with the electrokinetic data obtained for a range of hydrous Fe oxide catalysts (Doyle and Lyons 2013a, b, 2014a).

In the context of the current discussion, it is worth pointing out the molecular nature of these mechanisms. Essentially a modification of the Kobussen Pathway (Table 2.1) to take into account the nature of the surfaquo groups on the Fe surface, the mechanism in Fig. 2.17 also draws heavily on molecular concepts, including Fe (V) oxo catalysis (McDonald and Que 2011), and is analogous to those depicted for various homogeneous catalyst systems (Wang et al. 2010; Busch et al. 2011a, b; Duan et al. 2012). This is not unexpected given the very dispersed and somewhat tenuous nature of the catalytically active hydrous oxide layer. A common feature of these systems is a lack of any significant contribution to double-layer charging with increasing hydrous layer thickness indicating that a distinct oxide-solution interface is not present (Burke and Lyons 1986). In contrast, the electrocatalytic currents associated with these films often increase with layer thickness (Doyle and Lyons 2013a, b; O'Sullivan and Burke 1990), reflecting an increased concentration of active sites. As noted by O'Sullivan and Burke (1990), the behaviour of the open polymeric network is probably not greatly different from that of its oxymetal components. Thus, the hydrous oxide film may be regarded as surface bound polynuclear species consisting of linked surfaquo groups arranged in a dispersed three dimensional structure with each group being electrocatalytically active. Even in the case of the largely anhydrous thermal oxides, surfaquo group coverage can be considerable. Lyons and Burke (1987) have estimated that the fractional surfaquo group coverage on RuO_2 can reach as much as 30 %. Indeed, it has been noted that the origin of the electrocatalytic properties of thermally prepared RuO_2 films is not to be sought in the intrinsic rutile structure of the oxide, rather the catalytic

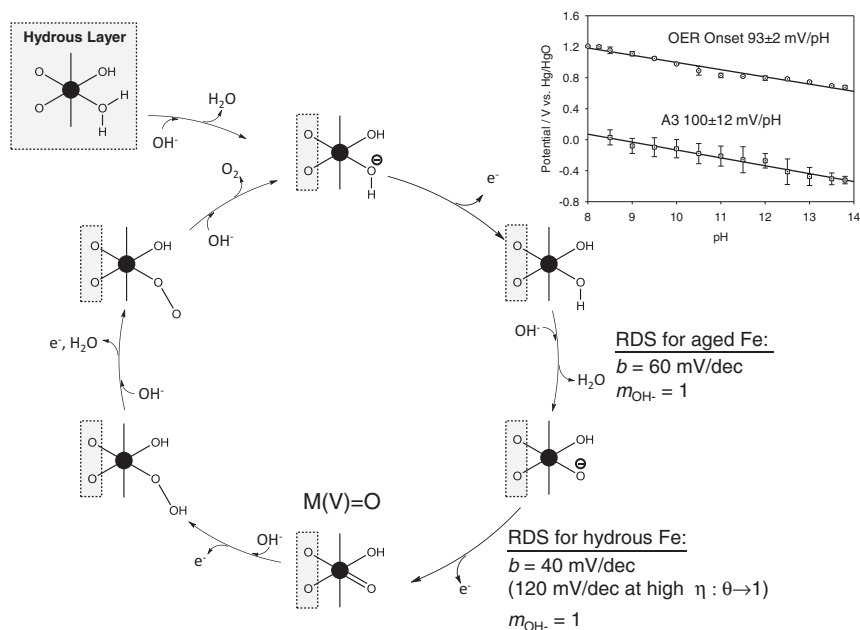


Fig. 2.17 Schematic representation of the mechanism for oxygen evolution at hydrous Fe oxides in alkaline media. Note that octahedrally co-ordinated oxymetal surfaquo groups are identified as the catalytically active species and are located throughout the hydrous layer. Deprotonation of co-ordinated water is assumed to be facile at high pH and so the reaction is initiated at co-ordinated hydroxide moieties. The inset shows the pH dependence of the OER onset potential and the hydrous oxide redox potential A3 associated with an Fe(II)/Fe(III) transition. Adapted from Doyle et al. (2013)

properties are more likely to originate from the state of surface atoms (Lodi et al. 1978). In this way, the surfaquo group is a potentially unifying concept, bringing together current understanding of the OER at various metal oxide catalysts while providing a bridge with the allied field of water oxidation in homogeneous catalytic systems via transition metal complexes.

While the direct spectroscopic determination of the structure and composition of these anionic entities has not been achieved, a number of properties underpinning the surfaquo group concept have been independently observed by other researchers. Hydrated surface structures have also been implicated as the catalytic active sites for the OER by the group of Nocera. These authors combined electrokinetic studies with detailed spectroscopic analysis to provide a mechanistic picture of the OER at several Co (Kanan and Nocera 2008; Surendranath et al. 2010; Kanan et al. 2010; McAlpin et al. 2010) Mn (Huynh et al. 2014) and Ni (Bediako et al. 2012, 2013) based oxygen evolution catalysts. X-ray absorption spectroscopy (XAS) studies of electrodeposited Co oxides showed that the catalyst films were composed of molecular cobaltate clusters (MCC) consisting of edge-sharing CoO_6 octahedra (Kanan et al. 2010). Specifically, oxygen isotope studies suggested that solvent

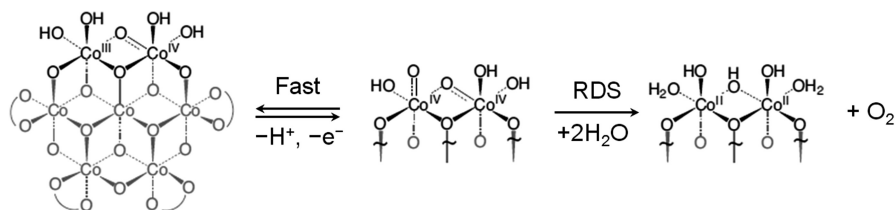


Fig. 2.18 Reaction pathway for the OER at CoPi films. A proton coupled electron transfer equilibrium is followed by a rate-determining O–O bond forming step. The structure of the MCC is shown on the left. Curved lines denote phosphate, OH_x or terminal bridging ligands. Adapted from Surendranath and Nocera (2012)

exposed Co centres at the edges of these MCCs were the active sites for oxygen evolution catalysis. Furthermore, X-ray absorption near-edge spectroscopy (XANES) (Kanan et al. 2010) and EPR (McAlpin et al. 2010) studies indicated that the resting state of the catalyst at potentials associated with active oxygen evolution—the high surface coverage species in the terminology of Sect. 2.2—was a mixed valent Co(III)/Co(IV) surface unit, as shown in Fig. 2.18. Similar octahedral mixed valent catalytic resting states have been proposed for electrodeposited Mn (Huynh et al. 2014) and Ni (Bediako et al. 2012) oxides as well as Ni–Fe mixed oxides (Trotchaud et al. 2014). On this basis, the key steps in the OER at the Co based catalysts involved the oxidation of hydroxylated surface Co(III)–OH units to Co(IV)–O moieties followed by slow O_2 evolution as part of a chemical rate-determining step (Surendranath et al. 2010), in agreement with the experimentally observed 60 mV dec^{-1} Tafel slope and reaction order $m_{\text{H}^+} = -1$.

The amorphisation of metal oxide surfaces has been observed by a number of research groups. Implicit in the surfaquo group description of the oxide surface is the presence of an amorphous oxide–solution interface irrespective of the crystallinity of the bulk oxide. In line with this, Lee et al. (2012) reported significant changes in the surface structure of lithium ion battery materials during oxygen evolution. Transmission electron microscopy (TEM) showed that the crystalline surface structure of LiCoPO_4 materials became progressively more amorphous with potential cycling under oxygen evolution conditions. At neutral pH, these structural changes correlated with a significant increase in OER current density. Using energy dispersive X-ray (EDX) spectroscopy coupled with scanning TEM it was found that the change in surface structure with potential cycling was accompanied by phosphorous leaching from the layer. In particular, the amorphous surface structure of the activated LiCoPO_4 was compositionally similar to that of the CoPi film, suggesting the increased activity could be attributed to the formation of hydrated molecular scale domains at the oxide–solution interface. Similar structural changes have also been observed for perovskite oxide catalysts. May et al. (2012) showed that a series of high activity perovskites such as BSCF and $\text{SrCo}_{0.8}\text{Fe}_{0.2}\text{O}_{3-\delta}$ can quickly undergo amorphisation of their surface at OER potentials. These structural changes were also accompanied by reduced surface concentrations of Ba^{2+} and Sr^{2+} ions as well as increased OER current densities. Interestingly, perovskites with

lower activities did not undergo similar structural changes, indicating that these amorphous surface structures play an important role in the catalytic activity of these oxides.

Certainly, knowledge of the chemical and structural properties of the surface oxide phase is important for a complete description of OER catalysis. As a whole, these studies highlight how restructuring of the oxide surface during the OER can lead to active chemistry which is significantly different from the bulk material. Understanding how these changes impact the OER activity is critical for the design of new and improved catalysts. In this regard, the surfaquo group concept offers a molecular like understanding of the activity of oxide catalysts; the amphoteric character of the anodic oxides implies that it is more realistic to view the OER active sites in terms of anionic surface complexes with molecular properties rather than the traditional viewpoint of stoichiometric units of the bulk oxide material. Within this framework catalyst design principles such as the hydrogen acceptor and partial-charge transfer models may be productively understood along the lines of well-established molecular concepts, such as intramolecular hydrogen bonding and electron withdrawing groups. Insights such as these, bridging the fields of homogeneous and heterogeneous OER catalysis, hold the key to further advancement in the mechanistic understanding of the OER and a more intuitive design of enhanced oxygen evolution catalysts.

2.6 Conclusion

The OER is a critical obstacle to the widespread development of a solar to fuel energy conversion infrastructure. Optimising the kinetics of the OER is crucial if the commercial potential of promising water-splitting technologies for the generation of hydrogen as a renewable fuel are to be maximised. Accordingly, the development of efficient, abundant, and inexpensive oxygen evolution catalysts is essential and the formulation of a function led design strategy would have a broad impact on renewable energy research.

The central challenge for oxygen evolution research is understanding the mechanistic details and structural motifs required for efficient catalysis. Catalyst design requires knowledge not only of the intrinsic activity of the catalytic material but also the structure and stability of the oxide surface. Significant breakthroughs will come only from an open-minded multidisciplinary approach. The OER remains a fundamental challenge for electrochemistry and a thorough electrokinetic analysis should underpin any mechanistic study of the OER. From this platform, a combined theoretical and spectroscopic study can provide vital insight into the reactive structures. Theoretical calculations have contributed significantly to our understanding of reactivity at well-defined oxides and will continue to be an important tool. But the active oxides are not well-defined, undergoing dynamic structural changes, and direct spectroscopic analysis of the reactive surface is currently lacking. In this respect it is envisaged that ongoing improvements in in-situ

spectroscopic techniques will be a major source of advancement in the understanding of structure–function relationships.

Ultimately, uncovering the structural and chemical features of the active site is the key to revealing oxygen evolution catalyst design principles. Throughout this chapter the discussion has signposted a move towards a microscopic consideration of catalyst activity in terms of the atomic or molecular scale properties of the layer. Certainly there is an emerging opinion that future developments in the study of the OER will come from the integration of the allied fields of heterogeneous surface and homogeneous molecular catalysis. Indeed, it seems that the molecular chemistry of the oxide–solution interface—the *surfaquo* group?—determines the chemistry of the oxygen evolution catalyst.

Acknowledgements The research described here has emanated in part from projects conducted with the financial support of Science Foundation Ireland (SFI) under grant number SFI/10/IN.1/I2969. RLD also wishes to acknowledge the Irish Research Council (IRC) for a Government of Ireland Postdoctoral Fellowship GOIPD/2014/120.

References

- Akimov AV, Muckerman JT, Prezhdo OV (2013) Nonadiabatic dynamics of positive charge during photocatalytic water splitting on GaN(10-10) surface: charge localization governs splitting efficiency. *J Am Chem Soc* 135:8682–8691
- Albery WJ (1975) *Electrode kinetics*. Clarendon, Oxford, p 41
- Balasubramanian M, Melendres CA, Mini S (2000) X-ray absorption spectroscopy studies of the local atomic and electronic structure of iron incorporated into electrodeposited hydrous nickel oxide films. *J Phys Chem B* 104:4300–4306
- Ballhausen CJ, Gray HB (1962) The electronic structure of the vanadyl ion. *Inorg Chem* 1:111–122
- Bard AJ, Faulkner LR (2000) *Electrochemical methods: fundamentals and applications*, 2nd edn. Wiley, New York, pp 87–136
- Bediako DK, Lassalle-Kaiser B, Surendranath Y, Yano J, Yachandra VK, Nocera DG (2012) Structure-activity correlations in a nickel-borate oxygen evolution catalyst. *J Am Chem Soc* 134:6801–6809
- Bediako DK, Surendranath Y, Nocera DG (2013) Mechanistic studies of the oxygen evolution reaction mediated by a nickel–borate thin film electrocatalyst. *J Am Chem Soc* 135:3662–3674
- Betley TA, Wu Q, Van Voorhis T, Nocera DG (2008) Electronic design criteria for O–O bond formation via metal-oxo complexes. *Inorg Chem* 47:1849–1861
- Bian W, Yang Z, Strasser P, Yang R (2014) A CoFe_2O_4 /graphene nanohybrid as an efficient bi-functional electrocatalyst for oxygen reduction and oxygen evolution. *J Power Sources* 250:196–203
- Bisquert J, Garcia-Belmonte G, Fabregat-Santiago F, Ferriols NS, Bogdanoff P, Pereira EC (2000a) Doubling exponent models for the analysis of porous film electrodes by impedance. Relaxation of TiO_2 nanoporous in aqueous solution. *J Phys Chem B* 104:2287–2298
- Bisquert J, Garcia Belmonte G, Fabregat Santiago F, Ferriols NS, Yamashita M, Pereira EC (2000b) Application of a distributed impedance model in the analysis of conducting polymer films. *Electrochem Commun* 2:601–605
- Bligaard T, Norskov JK (2007) Ligand effects in heterogeneous catalysis and electrochemistry. *Electrochim Acta* 52:5512–5516

- Bligaard T, Nørskov JK, Dahl S, Matthiesen J, Christensen CH, Sehested J (2004) The Brønsted-Evans-Polanyi relation and the volcano curve in heterogeneous catalysis. *J Catal* 224:206–217
- Bockris JO'M, Khan SUM (1993) *Surface electrochemistry*. Plenum Press, New York, pp 218–223
- Bockris JO'M, Otagawa T (1983) Mechanism of oxygen evolution on perovskites. *J Phys Chem* 87:2960–2971
- Bockris JOM, Otagawa T (1984) The electrocatalysis of oxygen evolution on perovskites. *J Electrochem Soc* 131:290–302
- Bockris JO'M, Reddy AKN, Gamboa-Aldeco M (2002) *Modern electrochemistry 2A*, 2nd edn. Kluwer Academic Publishers, New York, p 1412
- Bourgault PL, Conway BE (1960) The electrochemical behavior of the nickel oxide electrode. Part 2. Quasi-equilibrium behavior. *Can J Chem* 38:1557–1575
- Brimblecombe R, Dismukes GC, Swiegers GF, Spiccia L (2009) Molecular water oxidation catalysts for photoelectrochemical cells. *Dalton Trans* 43:9374–9384
- Burke LD, Lyons MEG (1986) The formation and stability of hydrous oxide films on iron under potential cycling conditions in aqueous solution at high pH. *J Electroanal Chem* 198:347–368
- Burke LD (1986) M.E.G. Lyons. In: Bockris JOM, White RE, Conway BE (eds) *Modern aspects of electrochemistry*, vol 18. Plenum Publ. Corp, New York, pp 169–248
- Burke LD, O'Sullivan EJM (1978) Enhanced oxide growth at a rhodium surface in base under potential cycling conditions. *J Electroanal Chem* 93:11–18
- Burke LD, O'Sullivan EJM (1981) Oxygen gas evolution on hydrous oxides – an example of three-dimensional electrocatalysis? *J Electroanal Chem* 117:155–160
- Burke LD, Twomey TAM (1984) Influence of the acid/base character of the surface on the electrocatalytic behavior of both nickel and nickel oxide anodes, with particular reference to oxygen gas evolution. *J Electroanal Chem* 167:285–290
- Burke LD, Whelan DP (1984) A voltammetric investigation of the charge storage reactions of hydrous iridium oxide layers. *J Electroanal Chem* 162:121–141
- Burke LD, Lyons MEG, O'Sullivan EJM, Whelan DP (1981) Influence of hydrolysis on the redox behavior of hydrous oxide films. *J Electroanal Chem* 122:403–407
- Burke LD, Lyons MEG, McCarthy M (1982a) Oxygen evolution and corrosion at ruthenium dioxide-based anodes. *Adv Hydrogen Energy* 3:267
- Burke LD, Lyons MEG, Whelan DP (1982b) Influence of pH on the reduction of thick anodic oxide films on gold. *J Electroanal Chem* 139:131–142
- Burke LD, Collins JA, Horgan MA, Hurley LM, O'Mullane AP (2000) The importance of the active states of surface atoms with regard to the electrocatalytic behaviour of metal electrodes in aqueous media. *Electrochim Acta* 45:4127–4134
- Burke LD, O'Connell AM, O'Mullane AP (2003) The role of defects, or active states, in surface electrochemistry with particular reference to gold in neutral solution. *J Appl Electrochem* 33:1125–1135
- Busch M, Ahlberg E, Panas I (2011a) Hydroxide oxidation and peroxide formation at embedded binuclear transition metal sites; TM = Cr, Mn, Fe, Co. *Phys Chem Chem Phys* 13:15062–15068
- Busch M, Ahlberg E, Panas I (2011b) Electrocatalytic oxygen evolution from water on a Mn (III–V) dimer model catalyst—A DFT perspective. *Phys Chem Chem Phys* 13:15069–15076
- Busch M, Ahlberg E, Panas I (2013a) Validation of binuclear descriptor for mixed transition metal oxide supported electrocatalytic water oxidation. *Catal Today* 202:114–119
- Busch M, Ahlberg E, Panas I (2013b) Water oxidation on MnO_x and IrO_x: why similar performance? *J Phys Chem C* 117:288–292
- Calle-Vallejo F, Inoglu NG, Su H-Y, Martinez JJ, Man IC, Koper MTM, Kitchin JR, Rossmeisl J (2013) Number of outer electrons as descriptor for adsorption processes on transition metals and their oxides. *Chem Sci* 4:1245–1249
- Calle-Vallejo F, Diaz-Morales O, Kolb M, Koper MTM (2015) Why Is bulk thermochemistry a good descriptor for the electrocatalytic activity of transition metal oxides? *ACS Catal* 5:869–873

- Carugati A, Lodi G, Trasatti S (1981) Fractional reaction orders in oxygen evolution from acidic solutions at ruthenium oxide anodes. *Mater Chem* 6:255–266
- Chang SH, Danilovic N, Chang K-C, Subbaraman R, Paulikas AP, Fong DD, Highland MJ, Baldo PM, Stamenkovic VR, Freeland JW, Eastman JA, Markovic NM (2014) Functional links between stability and reactivity of strontium ruthenate single crystals during oxygen evolution. *Nat Commun* 5:4191–4199
- Chang SH, Connell JG, Danilovic N, Subbaraman R, Chang K-C, Stamenkovic VR, Markovic NM (2015) Activity–stability relationship in the surface electrochemistry of the oxygen evolution reaction. *Faraday Discuss* 176:125–133
- Chen JG, Menning CA, Zellner MB (2008) Monolayer bimetallic surfaces: experimental and theoretical studies of trends in electronic and chemical properties. *Surf Sci Rep* 63:201–254
- Conway BE (1995) Electrochemical oxide film formation at noble metals as a surface-chemical process. *Prog Surf Sci* 49:331–452
- Conway BE, Bourgault PL (1962) Significance of E.M.F. decay measurements. Applications to the nickel oxide electrode. *Trans Faraday Soc* 58:593–607
- Conway BE, Bourgault PL (1959) The electrochemical behavior of the nickel – nickel oxide electrode part 1. Kinetics of self-discharge. *Can J Chem* 37:292–307
- Conway BE, Salomon M (1964) Electrochemical reaction orders: applications to the hydrogen- and oxygen-evolution reactions. *Electrochim Acta* 9:1599–1615
- Conway BE, Gileadi E (1962) Kinetic theory of pseudo-capacitance and electrode reactions at appreciable surface coverage. *Trans Faraday Soc* 58:2493–2509
- Conway BE, Bai L, Sattar MA (1987) Role of the transfer coefficient in electrocatalysis: applications to the H₂ and O₂ evolution reactions and the characterization of participating adsorbed intermediates. *Int J Hydrogen Energy* 12:607–621
- Corrigan DA (1987) The catalysis of the oxygen evolution reaction by iron impurities in thin film nickel oxide electrodes. *J Electrochem Soc* 134:377–384
- Corrigan DA, Conell RS, Fierro CA, Scherson DA (1987) In situ mossbauer study of redox processes in a composite hydroxide of iron and nickel. *J Phys Chem* 91:5009–5011
- Crabtree GW, Dresselhaus MS, Buchanan MV (2004) The hydrogen economy. *Phys Today* 57:39–44
- Damjanovic A, Dey A, Bockris JO'M (1966) Kinetics of oxygen evolution and dissolution on platinum electrodes. *Electrochim Acta* 11:791–814
- Damjanovic A, Genshaw MA, Bockris JO'M (1967a) The role of hydrogen peroxide in oxygen reduction at platinum in H₂SO₄ solution. *J Electrochem Soc* 114:466–472
- Damjanovic A, Genshaw MA, Bockris JO'M (1967b) The mechanism of oxygen reduction at platinum in alkaline solutions with special reference to H₂O₂. *J Electrochem Soc* 114:1107–1112
- Danilovic N, Subbaraman R, Chang K-C, Chang SH, Kang Y, Snyder J, Paulikas AP, Strmcnik D, Kim YT, Myers D, Stamenkovic VR, Markovic NM (2014a) Using surface segregation to design stable Ru-Ir oxides for the oxygen evolution reaction in acidic environments. *Angew Chem Int Ed* 53:14016–14021
- Danilovic N, Subbaraman R, Chang K-C, Chang SH, Kang YJ, Snyder J, Paulikas AP, Strmcnik D, Kim Y-T, Myers D, Stamenkovic VR, Markovic NM (2014b) Activity–stability trends for the oxygen evolution reaction on monometallic oxides in acidic environments. *J Phys Chem Lett* 5:2474–2478
- Dau H, Limberg C, Reier T, Risch M, Roggan S, Strasser P (2010) The mechanism of water oxidation: from electrolysis via homogeneous to biological catalysis. *ChemCatChem* 2:724–761
- Desilvestro J, Corrigan DA, Weaver MJ (1986) Spectroelectrochemistry of thin nickel hydroxide films on gold using surface-enhanced raman spectroscopy. *J Phys Chem* 90:6408–6411
- Diaz-Morales O, Calle-Vallejo F, de Munck C, Koper MTM (2013) Electrochemical water splitting by gold: evidence for an oxide decomposition mechanism. *Chem Sci* 4:2334–2343
- Dinga GP (1985) Hydrogen: the ultimate fuel and energy carrier. *J Chem Ed* 65:688–691

- Doyle RL, Lyons MEG (2013a) Kinetics and mechanistic aspects of the oxygen evolution reaction at hydrous iron oxide films in base. *J Electrochem Soc* 160:H142–H154
- Doyle RL, Lyons MEG (2013b) An electrochemical impedance study of the oxygen evolution reaction at hydrous iron oxide in base. *Phys Chem Chem Phys* 15:5224–5237
- Doyle RL, Lyons MEG (2014a) Redox and oxygen evolution properties of nafion and single walled carbon nanotube/hydrous iron oxide composite films. *Electrocatalysis* 5:114–124
- Doyle RL, Lyons MEG (2014b) The mechanism of oxygen evolution at superactivated gold electrodes in aqueous alkaline solution. *J Solid State Electrochem* 18:3271–3286
- Doyle RL, Godwin IJ, Brandon MP, Lyons MEG (2013) Redox and electrochemical water splitting catalytic properties of hydrated metal oxide electrodes. *Phys Chem Chem Phys* 15:13737–13783
- Duan L, Bozoglian F, Mandal S, Stewart B, Privalov T, Llobet A, Sun L (2012) A molecular ruthenium catalyst with water-oxidation activity comparable to that of photosystem II. *Nature* 441:418–423
- Dumesic JA, Huber GW, Boudart M (2008) In: Ertl G, Knözinger H, Schüth F, Weitkamp J (eds) *Handbook of heterogeneous catalysis*, 2nd edn. Wiley, Weinheim, p 1445
- Egdell RG, Goodenough JB, Hamnett A, Naish CJ (1983) Electrochemistry of ruthenates part 1. Oxygen reduction on pyrochlore ruthenates. *J Chem Soc Faraday Trans* 79:893–912
- El-Deab MS, Awad MI, Mohammad AM, Ohsaka T (2007) Enhanced water electrolysis: electrocatalytic generation of oxygen gas at manganese oxide nanorods modified electrodes. *Electrochem Commun* 9:2082–2087
- Fabbri E, Haberer A, Waltar K, Kötz R, Schmidt TJ (2014) Developments and perspectives of oxide-based catalysts for the oxygen evolution reaction. *Catal Sci Technol* 4:3800–3821
- Fachinotti E, Guerrini E, Tavares AC, Trasatti S (2007) Electrocatalysis of H₂ evolution by thermally prepared ruthenium oxide. Effect of precursors: Nitrate vs. chloride. *J Electroanal Chem* 600:103–112
- Farrow CL, Bediako DK, Surendranath Y, Nocera DG, Billinge SJL (2013) Intermediate-range structure of self-assembled cobalt-based oxygen-evolving catalyst. *J Am Chem Soc* 135:6403–6406
- Frydendal R, Busch M, Halck NB, Paoli EA, Krttil P, Chorkendorff I, Rossmeisl J (2015) Enhancing activity for the oxygen evolution reaction: the beneficial interaction of gold with manganese and cobalt oxides. *ChemCatChem* 7:149–154
- Galán-Mascarós JR (2015) Water oxidation at electrodes modified with earth-abundant transition-metal catalysts. *ChemElectroChem* 2:37–50
- García-Mota M, Vojvodic A, Metiu H, Man IC, Su H-Y, Rossmeisl J, Nørskov JK (2011) Tailoring the activity for oxygen evolution electrocatalysis on Rutile TiO₂(110) by transition-metal substitution. *ChemCatChem* 3:1607–1611
- Gileadi E (1993) *Electrode Kinetics*, VCH, New York, pp 140–144
- Godwin IJ, Doyle RL, Lyons MEG (2014) The mechanism of oxygen reactions at porous oxide electrodes III. Water oxidation catalysis at RuO₂/NiO mixed oxide electrodes. *J Electrochem Soc* 161:F906–F917
- Gong M, Li Y, Wang H, Liang Y, Wu JZ, Zhou J, Wang J, Regier T, Wei F, Dai H (2013) An advanced Ni-Fe layered double hydroxide electrocatalyst for water oxidation. *J Am Chem Soc* 135:8452–8455
- Gorlin Y, Chung C-J, Benck JD, Nordlund D, Seitz L, Weng T-C, Sokaras D, Clemens BM, Jaramillo TF (2014) Understanding interactions between manganese oxide and gold that lead to enhanced activity for electrocatalytic water oxidation. *J Am Chem Soc* 136:4920–4926
- Grätzel M (2005) Mesoscopic solar cells for electricity and hydrogen production from sunlight. *Chem Lett* 34:8–13
- Greeley J, Markovic NM (2012) The road from animal electricity to green energy: combining experiment and theory in electrocatalysis. *Energy Environ Sci* 5:9246–9256
- Guerrini E, Chen H, Trasatti S (2007) Oxygen evolution on aged IrO_x/Ti electrodes in alkaline solutions. *J Solid State Electrochem* 11:939–945

- Guidelli R, Compton RG, Feliu JM, Gileadi E, Lipkowsky J, Schmickler W, Trasatti S (2014a) Defining the transfer coefficient in electrochemistry: an assessment (IUPAC Technical Report). *Pure Appl Chem* 86:245–258
- Guidelli R, Compton RG, Feliu JM, Gileadi E, Lipkowsky J, Schmickler W, Trasatti S (2014b) Definition of the transfer coefficient in electrochemistry (IUPAC Recommendations 2014). *Pure Appl Chem* 86:259–262
- Halck NB, Petrykin V, Krtil P, Rossmeisl J (2014) Beyond the volcano limitations in electrocatalysis - oxygen evolution reaction. *Phys Chem Chem Phys* 16:13682–13688
- Hall DE (1983) Ni(OH)₂-impregnated anodes for alkaline water electrolysis. *J Electrochem Soc* 130:317–321
- Hansen HA, Man IC, Studt F, Abild-Pedersen F, Bligaard T, Rossmeisl J (2010) Electrochemical chlorine evolution at Rutile oxide 110 surfaces. *Phys Chem Chem Phys* 12:283–290
- Harrington DA, van den Driessche P (2011) Mechanism and equivalent circuits in electrochemical impedance spectroscopy. *Electrochim Acta* 56:8005–8013
- Häussinger P, Lohmüller R, Watson AM (2000) Ullmann's encyclopedia of industrial chemistry. Wiley, Weinheim
- Hoare JP (1967) Oxygen electrode on noble metals. *Adv Electrochem Electrochem Eng* 6:201–288
- Hoare JP (1968) The electrochemistry of oxygen. Interscience, New York, pp 82–91
- Hrussanova A, Guerrini E, Trasatti S (2004) Thermally prepared Ti/RhOx electrodes IV: O₂ evolution in acid solution. *J Electroanal Chem* 564:151–157
- Huynh M, Bediako DK, Nocera DG (2014) A functionally stable manganese oxide oxygen evolution catalyst in acid. *J Am Chem Soc* 136:6002–6010
- Inoglu N, Kitchin JR (2011) Identification of sulfur-tolerant bimetallic surfaces using DFT parametrized models and atomistic thermodynamics. *ACS Catal* 1:399–407
- Joya KS, Joya YF, Ocakoglu K, van de Krol R (2013) Water-splitting catalysis and solar fuel devices: artificial leaves on the move. *Angew Chem Int Ed* 52:10426–10437
- Kanan MW, Nocera DG (2008) In situ formation of an oxygen-evolving catalyst in neutral water containing phosphate and Co²⁺. *Science* 321:1072–1075
- Kanan MW, Yano J, Surendranath Y, Dinca M, Yachandra VK, Nocera DG (2010) Structure and valency of a cobalt–phosphate water oxidation catalyst determined by in situ X-ray spectroscopy. *J Am Chem Soc* 132:13692–13701
- Katsounaros I, Cherevko S, Zeradjanin AR, Mayrhofer KJ (2014) Oxygen electrochemistry as a cornerstone for sustainable energy conversion. *J Angew Chem Int Ed* 53:102–121
- Kharche N, Hybersten MS, Muckerman JT (2014) Computational investigation of structural and electronic properties of aqueous interfaces of GaN, ZnO, and a GaN/ZnO alloy. *Phys Chem Chem Phys* 16:12057–12066
- Kim S, Tryk DA, Antonio MR, Carr R, Scherson DJ (1994) In situ X-ray absorption fine structure studies of foreign metal ions in nickel hydrous oxide electrodes in alkaline electrolytes. *Phys Chem* 98:10269–10276
- Kim TW, Choi K-S (2014) Nanoporous BiVO₄ photoanodes with dual-layer oxygen evolution catalysts for solar water splitting. *Science* 343:990–994
- Kinoshita K (1992) Electrochemical oxygen technology. Wiley, New York
- Klahr B, Gimenez S, Fabregat-Santiago F, Hamann T, Bisquert J (2012a) Water oxidation at hematite photoelectrodes: the role of surface states. *J Am Chem Soc* 134:4294–4302
- Klahr B, Gimenez S, Fabregat-Santiago F, Bisquert J, Hamann TW (2012b) Photoelectrochemical and impedance spectroscopic investigation of water oxidation with “Co-Pi”-coated hematite electrodes. *J Am Chem Soc* 134:16693–16700
- Kobussen AGC, Broers GHJ (1981) The oxygen evolution on La_{0.5}Ba_{0.5}CoO₃: theoretical impedance behaviour for a multi-step mechanism involving two adsorbates. *J Electroanal Chem* 126:221–240
- Koper MTM (2011) Thermodynamic theory of multi-electron transfer reactions: implications for electrocatalysis. *J Electroanal Chem* 660:254–260

- Koper MTM (2013) Analysis of electrocatalytic reaction schemes: distinction between rate-determining and potential-determining steps. *J Solid State Electrochem* 17:339–344
- Koper MTM, Heering HA (2010) In: Wiekowski JKNA (ed) *Fuel cell science: theory, fundamentals and bio-catalysis*. Wiley, New York, pp 71–110
- Krasil'shchikov AI (1963) Intermediate stages in the anodic evolution of oxygen. *Zh Fiz Khim* 37:531
- Landon J, Demeter E, Inoglu N, Keturakis C, Wachs IE, Vasic R, Frenkel AI, Kitchin JR (2012) Spectroscopic characterization of mixed Fe–Ni oxide electrocatalysts for the oxygen evolution reaction in alkaline electrolytes. *ACS Catal* 2:1793–1801
- Lee DU, Kim BJ, Chen ZW (2013) One-pot synthesis of a mesoporous NiCo₂O₄ nanoplatelet and graphene hybrid and its oxygen reduction and evolution activities as an efficient bi-functional electrocatalyst. *J Mater Chem A* 1:4754–4762
- Lee SW, Carlton C, Risch M, Surendranath Y, Chen S, Furutsuki S, Yamada A, Nocera DG, Shao-Horn Y (2012) The nature of lithium battery materials under oxygen evolution reaction conditions. *J Am Chem Soc* 134:16959–16962
- Lewis NS, Nocera DG (2006) Powering the planet: chemical challenges in solar energy utilization. *Proc Natl Acad Sci U S A* 103:15729–15735
- Liang YY, Li YG, Wang HL, Zhou JG, Wang J, Regier T, Dai HJ (2011) Co₃O₄ nanocrystals on graphene as a synergistic catalyst for oxygen reduction reaction. *Nat Mater* 10:780–786
- Liang YY, Wang HL, Zhou JG, Li YG, Wang J, Regier T, Dai HJ (2012) Covalent hybrid of spinel manganese-cobalt oxide and graphene as advanced oxygen reduction electrocatalysts. *J Am Chem Soc* 134:3517–3523
- Liao P, Keith JA, Carter EA (2012) Water oxidation on pure and doped hematite (0001) surfaces: prediction of Co and Ni as effective dopants for electrocatalysis. *J Am Chem Soc* 134:13296–13309
- Lodi G, Sivieri E, De Battisti A, Trasatti S (1978) Ruthenium dioxide-based film electrodes. III. Effect of chemical composition and surface morphology on oxygen evolution in acid solutions. *J Appl Electrochem* 8:135–143
- Louie MW, Bell AT (2013) An investigation of thin-film Ni–Fe oxide catalysts for the electrochemical evolution of oxygen. *J Am Chem Soc* 135:12329–12337
- Lu X, Ng YH, Zhao C (2014) Gold nanoparticles embedded within mesoporous cobalt oxide enhance electrochemical oxygen evolution. *ChemSusChem* 7:82–86
- Lyons MEG, Brandon MP (2009) Redox switching and oxygen evolution electrocatalysis in polymeric iron oxyhydroxide films. *Phys Chem Chem Phys* 11:2203–2217
- Lyons MEG, Brandon MP (2010) A comparative study of the oxygen evolution reaction on oxidised nickel, cobalt and iron electrodes in base. *J Electroanal Chem* 641:119–130
- Lyons MEG, Burke LD (1987) Mechanism of oxygen reactions at porous oxide electrodes. Part 1. Oxygen evolution at ruthenium dioxide and ruthenium tin oxide (Ru_xSn_{1-x}O₂) electrodes in alkaline solution under vigorous electrolysis conditions. *J Chem Soc Faraday Trans* 83:299–321
- Lyons MEG, Floquet S (2011) Mechanism of oxygen reactions at porous oxide electrodes. Part 2—Oxygen evolution at RuO₂, IrO₂ and Ir_xRu_{1-x}O₂ electrodes in aqueous acid and alkaline solution. *Phys Chem Chem Phys* 13:5314–5335
- Lyons MEG, Doyle RL, Brandon MP (2011) Redox switching and oxygen evolution at oxidized metal and metal oxide electrodes: iron in base. *Phys Chem Chem Phys* 13:21530–21551
- Lyons MEG, Russell L, O'Brien M, Doyle RL, Godwin I, Brandon MP (2012a) Redox switching and oxygen evolution at hydrous oxy-hydroxide modified nickel electrodes in aqueous alkaline solution: effect of hydrous oxide thickness and base concentration. *Int J Electrochem Sci* 7:2710–2763
- Lyons MEG, Cakara A, O'Brien P, Godwin I, Doyle RL (2012b) Redox, pH sensing and electrolytic water splitting properties of electrochemically generated nickel hydroxide thin films in aqueous alkaline solution. *Int J Electrochem Sci* 7:11768–11795

- Lyons MEG, Doyle RL, Fernandez D, Godwin IJ, Browne MP, Rovetta A (2014) The mechanism and kinetics of electrochemical water oxidation at oxidised metal and metal oxide electrodes. Part 2. The surfaquo group mechanism. A mini review. *Electrochem Commun* 45:56–59
- Man IC, Su H-Y, Calle-Vallejo F, Hansen HA, Martinez JI, Inoglu NG, Kitchin J, Jaramillo TF, Nørskov JK, Rossmeisl J (2011) Universality in oxygen evolution electrocatalysis on oxide surfaces. *ChemCatChem* 3:1159–1165
- Marinia S, Salvi P, Nelli P, Pesentia R, Villa M, Berrettoni M, Zangaric G, Kiros Y (2012) Advanced alkaline water electrolysis. *Electrochim Acta* 82(384–391)
- Markovic NM, Ross PN (2002) Surface science studies of model fuel cell electrocatalysts. *Surf Sci Rep* 45:121–229
- Marx D, Tuckerman ME, Hutter J, Parrinello M (1999) The nature of the hydrated excess proton in water. *Nature* 397:601–604
- Matsumoto Y, Sato E (1986) Electrocatalytic properties of transition metal oxides for oxygen evolution reaction. *Mater Chem Phys* 14:397–426
- Mavrikakis M, Hammer B, Nørskov JK (1998) Effect of strain on the reactivity of metal surfaces. *Phys Rev Lett* 81:2819–2822
- May KJ, Carlton CE, Stoerzinger KA, Risch M, Suntivich J, Lee Y-L, Grimaud A, Shao-Horn Y (2012) The influence of oxygen evolution upon water oxidation on the surface of perovskite oxide catalysts. *J Phys Chem Lett* 3:3264–3270
- McAlpin JG, Surendranath Y, Dinca M, Stich TA, Stoian SA, Casey WH, Nocera DG, Britt RD (2010) EPR evidence for Co(IV) species produced during water oxidation at neutral pH. *J Am Chem Soc* 132:6882–6883
- McCrorry CCL, Jung SH, Peters JC, Jaramillo TF (2013) Benchmarking heterogeneous electrocatalysts for the oxygen evolution reaction. *J Am Chem Soc* 135:16977–16987
- McDonald AR, Que L (2011) Iron–oxo complexes: elusive iron(V) species identified. *Nature* 3:761–762
- McDonald JJ, Conway BE (1962) The role of surface films in the kinetics of oxygen evolution at Pd + Au alloy electrodes. *Proc Roy Soc Lond A* 269:419–440
- Merrill MD, Dougherty RC (2008) Metal oxide catalysts for the evolution of O₂ from H₂O. *J Phys Chem C* 112:3655–3666
- Meyer RE (1960) Cathodic processes on passive zirconium. *J Electrochem Soc* 107:847–853
- Michas A, Andolfatto F, Lyons MEG, Durand R (1992) Gas evolution reactions at conductive metallic oxide electrodes for solid polymer electrolyte water electrolysis. *Key Eng Mater* 72–74:535–549
- Mohammad AM, Awad MI, El-Deab MS, Okajima T, Ohsaka T (2008) Electrocatalysis by nanoparticles: optimisation of the loading level and operating pH for the oxygen evolution at crystallographically orientated manganese oxide nanorods modified electrodes. *Electrochim Acta* 53:4351–4358
- Montoya JH, Garcia-Mota M, Nørskov JK, Vojvodic A (2015) Theoretical evaluation of the surface electrochemistry of perovskites with promising photon absorption properties for solar water splitting. *Phys Chem Chem Phys* 17:2634–2640
- Nocera DG (2012) The artificial leaf. *Acc Chem Res* 45:767–776
- Nørskov JK, Bligaard T, Hvolbaek B, Abild-Petersen F, Chorkendorff I, Christensen CH (2008) The nature of the active site in heterogeneous metal catalysis. *Chem Soc Rev* 37:2163–2171
- Nørskov JK, Bligaard T, Rossmeisl J, Christensen CH (2009) Towards the computational design of solid catalysts. *Nat Chem* 1:37–46
- Novell-Leruth G, Carchini G, López N (2013) On the properties of binary rutile MO₂ compounds, M = Ir, Ru, Sn, and Ti: A DFT study. *J Chem Phys* 138:194706–194715
- Nowicka AM, Hasse U, Sievers G, Donten M, Stojek Z, Fletcher S, Scholz F (2010) Selective knockout of gold active sites. *Angew Chem Int Ed* 49:3006–3009
- O’Grady W, Iwakura C, Huang J, Yeager E (1974) In: Breiter MW (ed) *Proceedings of the symposium on electrocatalysis*. The Electrochemical Society Inc., Pennington, NJ, p 286
- Ohi J (2005) Hydrogen energy cycle: an overview. *J Mater Res* 20:3180–3187

- O'Sullivan EJM, Burke LD (1990) Kinetics of oxygen gas evolution on hydrous rhodium oxide films. *J Electrochem Soc* 137:466–471
- Parsons R (1951) General equations for the kinetics of electrode processes. *Trans Faraday Soc* 47:1332–1344
- Parsons R (1958) Rate of electrolytic hydrogen evolution and the heat of adsorption of hydrogen. *Trans Faraday Soc* 54:1053–1063
- Parsons R (1961) In: Delahay P (ed) *Advances in electrochemistry and electrochemical engineering*, vol 1. Interscience, New York, p 1
- Petrykin V, Macounova K, Shlyakhtin OA, Krtil P (2010) Tailoring the selectivity for electrocatalytic oxygen evolution on ruthenium oxides by zinc substitution. *Angew Chem Int Ed* 49:4813–4815
- Pourbaix M (1974) *Atlas of electrochemical equilibria in aqueous solutions*, 2nd edn. National Association of Corrosion Engineers, Houston, TX
- Rebouillat S, Lyons MEG, Brandon MP, Doyle RL (2011) Paving the way to the integration of smart nanostructures Part 2 - Nanostructured metal oxides for electrocatalysis and energy conversion. *Int J Electrochem Sci* 6:5830–5917
- Reier T, Oezaslan M, Strasser P (2012) Electrocatalytic Oxygen Evolution Reaction (OER) on Ru, Ir, and Pt catalysts: a comparative study of nanoparticles and bulk materials. *ACS Catal* 2:1765–1772
- Rios E, Chartier P, Gautier JL (1999) Oxygen evolution electrocatalysis in alkaline medium at thin $\text{Mn}_x\text{Co}_{3-x}\text{O}_4$ ($0 \leq x \leq 1$) spinel films on glass/SnO₂:F prepared by spray pyrolysis. *Solid State Sci* 1:267–277
- Rossmeisl J (2013) In: Schlögl R (ed) *Chemical energy storage*. De Gruyter Graduate, Berlin, pp 151–162
- Rossmeisl J, Logadottir A, Nørskov JK (2005) Electrolysis of water on (oxidized) metal surfaces. *Chem Phys* 319:178–184
- Rossmeisl J, Qu Z-W, Zhu H, Kroes G-J, Nørskov JK (2007a) Electrolysis of water on oxide surfaces. *J Electroanal Chem* 607:83–89
- Rossmeisl J, Dimitrievski K, Siegbahn P, Nørskov JK (2007b) Comparing electrochemical and biological water splitting. *J Phys Chem C* 111:18821–18823
- Rossmeisl J, Karlberg GS, Jaramillo T, Nørskov JK (2008) Steady state oxygen reduction and cyclic voltammetry. *Faraday Discuss* 140:337–346
- Ruban AV, Skriver HL, Nørskov JK (1999) Surface segregation energies in transition-metal alloys. *Phys Rev B* 59:15990–16000
- Ruetschi P, Delahay P (1955) Potential at zero charge for reversible and ideal polarized electrodes. *J Chem Phys* 23:697–699
- Sabatier P (1911) Hydrogenation and dehydrogenation by catalysis. *Ber Dtsch Chem Ges* 44:1984–2001
- Sato N (1998) *Electrochemistry at metal and semiconductor electrodes*. Elsevier, Amsterdam, pp 181–184
- Schlögl R (2010) The role of chemistry in the energy challenge. *ChemSusChem* 3:209–222
- Schwab GM (1981) In: Anderson JR, Boudart M (eds) *Catalysis – science and technology*, vol 2. Springer, Berlin, p 4
- Schweitzer GK, Pesterfield LL (2010) *The aqueous chemistry of the elements*. Oxford University Press, Oxford
- Shen X, Small YA, Wang J, Allen PB, Fernandez-Serra MV, Hybertsen MS, Muckerman JT (2010) Photocatalytic water oxidation at the GaN (1010) – water interface. *J Phys Chem C* 114:13695–13704
- Sheng WC, Gasteiger HA, Shao-Horn Y (2010) Hydrogen oxidation and evolution reaction kinetics on platinum: acid vs alkaline electrolytes. *J Electrochem Soc* 157:B1529–B1536
- Singh NK, Tiwari SK, Anitha KL, Singh RN (1996) Electrocatalytic properties of spinel-type $\text{Mn}_x\text{Fe}_{3-x}\text{O}_4$ synthesized below 100°C for oxygen evolution in KOH solutions. *J Chem Soc Faraday Trans* 92:2397–2400

- Smith RDL, Prévot MS, Fagan RD, Zhang Z, Sedach PA, Siu MKJ, Trudel S, Berlinguette CP (2013a) Photochemical route for accessing amorphous metal oxide materials for water oxidation catalysis. *Science* 340:60–63
- Smith RDL, Prévot MS, Fagan RD, Trudel S, Berlinguette CP (2013b) Water oxidation catalysis: electrocatalytic response to metal stoichiometry in amorphous metal oxide films containing iron, cobalt, and nickel. *J Am Chem Soc* 135:11580–11586
- Somorjai GA (1996) Modern surface science and surface technologies: an introduction. *Chem Rev* 96:1223–1235
- Su H-Y, Gorlin Y, Man IC, Calle-Vallejo F, Nørskov JK, Jaramillo TF, Rossmeisl J (2012) Identifying active surface phases for metal oxide electrocatalysts: a study of manganese oxide bi-functional catalysts for oxygen reduction and water oxidation catalysis. *Phys Chem Chem Phys* 14:14010–14022
- Subbaraman R, Tripkovic D, Chang K-C, Strmcnik D, Paulikas AP, Hirunsit P, Chan M, Greeley J, Stamenkovic V, Markovic NM (2012) Trends in activity for the water electrolyser reactions on 3d M(Ni,Co,Fe,Mn) hydr(oxy)oxide catalysts. *Nat Mater* 11:550–557
- Sun K, Kohyama M, Tanaka S, Takeda S (2012) Theoretical study of atomic oxygen on gold surface by Hückel theory and DFT calculations. *J Phys Chem A* 116:9568–9573
- Suntivich J, May KJ, Gasteiger H, Goodenough JB, Shao-Horn Y (2011) A perovskite oxide optimized for oxygen evolution catalysis from molecular orbital principles. *Science* 334:1383–1385
- Surendranath Y, Nocera DG (2012) Progress. In: Karlin KD (ed) *Inorganic chemistry*, vol 57. Wiley, New York, pp 505–560
- Surendranath Y, Kanan MW, Nocera DG (2010) Mechanistic studies of the oxygen evolution reaction by a cobalt-phosphate catalyst at neutral pH. *J Am Chem Soc* 132:16501–16509
- Tafel J (1904) Polarization in cathodic hydrogen evolution. *Z Phys Chem* 50:641–712
- Taylor HS (1925) A theory of the catalytic surface. *Proc Roy Soc Lond A* 108:105–111
- Terezo AJ, Bisquert J, Pereira EC, Garcia-Belmonte G (2001) Separation of transport, charge storage and reaction processes of porous electrocatalytic IrO₂ and IrO₂/Nb₂O₅ electrodes. *J Electroanal Chem* 508:59–69
- Thomas JGN (1961) Kinetics of electrolytic hydrogen evolution and the adsorption of hydrogen by metals. *Trans Faraday Soc* 57:1603–1611
- Trasatti S (1980) Electrocatalysis by oxides - attempt at a unifying approach. *J Electroanal Chem* 111:125–131
- Trasatti S (1984) Electrocatalysis in the anodic evolution of oxygen and chlorine. *Electrochim Acta* 29:1503–1512
- Trasatti S (1994) In: Lipkowsky J, Ross PN (eds) *Electrochemistry of novel materials*. VCH, New York, pp 207–295
- Tributsch H (2008) Photovoltaic hydrogen generation. *Int J Hydrogen Energy* 33:5911–5930
- Trotochaud L, Ranney JK, Williams KN, Boettcher SW (2012) Solution-cast metal oxide thin film electrocatalysts for oxygen evolution. *J Am Chem Soc* 134:17253–17261
- Trotochaud L, Young SL, Ranney JK, Boettcher SW (2014) Nickel-iron oxyhydroxide oxygen-evolution electrocatalysts: the role of intentional and incidental iron incorporation. *J Am Chem Soc* 136:6744–6753
- Tuckerman M, Laasonen K, Sprik M, Parrinello M (1995) Ab initio molecular dynamics simulation of the solvation and transport of hydronium and hydroxyl ions in water. *J Chem Phys* 103:150–161
- Turner JA (2004) Sustainable hydrogen production. *Science* 305:972–974
- Valdés Á, Qu Z-W, Kroes G-J, Rossmeisl J, Nørskov JK (2008) Oxidation and photo-oxidation of water on TiO₂ surface. *J Phys Chem C* 112:9872–9879
- Valdés Á, Brillet J, Grätzel M, Gudmundsdóttir H, Hansen HA, Jónsson H, Klüpfel P, Kroes G-J, Le Formal F, Man IC, Martins RS, Nørskov JK, Rossmeisl J, Sivula K, Vojvodic A, Zäch M (2012) Solar hydrogen production with semiconductor metal oxides: new directions in experiment and theory. *Phys Chem Chem Phys* 14:49–70

- Vassilev P, Koper MTM, van Santen RA (2002) Ab initio molecular dynamics of hydroxyl-water coadsorption on Rh(111). *Chem Phys Lett* 359:337–342
- Viswanathan V, Pickrahn KL, Luntz AC, Bent SF, Nørskov JK (2014) Nanoscale limitations in metal oxide electrocatalysts for oxygen evolution. *Nano Lett* 14:5853–5857
- Wang L, Zhao X, Lu Y, Xu M, Zhang D, Ruoff RS, Stevenson KJ, Goodenough JB (2011) CoMn_2O_4 spinel nanoparticles grown on graphene as bifunctional catalyst for lithium-air batteries. *J Electrochem Soc* 158:A1379–A1382
- Wang L-P, Wu Q, Van Voorhis T (2010) Acid-base mechanism for ruthenium water oxidation catalysts. *Inorg Chem* 49:4543–4553
- Willems H, Kobussen AGC, De Wit JHW, Broers GHJ (1984) The oxygen evolution reaction on cobalt. Part 1. Reaction order experiments and impedance measurements. *J Electroanal Chem* 170:227–242
- Yeo BS, Bell AT (2011) Enhanced activity of gold-supported cobalt oxide for the electrochemical evolution of oxygen. *J Am Chem Soc* 133:5587–5593
- Yeo BS, Bell AT (2012) In situ raman study of nickel oxide and gold-supported nickel oxide catalysts for the electrochemical evolution of oxygen. *J Phys Chem C* 116:8394–8400
- Zeng K, Zhang D (2010) Recent progress in alkaline water electrolysis for hydrogen production and applications. *Prog Energy Combust Sci* 36:307–326
- Zhou L (2005) Progress and problems in hydrogen storage methods. *Renew Sustain Energy Rev* 9:395–408

<http://www.springer.com/978-3-319-29639-5>

Photoelectrochemical Solar Fuel Production

From Basic Principles to Advanced Devices

Giménez, S.; Bisquert, J. (Eds.)

2016, XXI, 559 p. 244 illus., 148 illus. in color.,

Hardcover

ISBN: 978-3-319-29639-5